UCLouvain

École polytechnique de Louvain

Joint evaluation of performance and environmental impacts of a microfabricated device

Author: **Tom Van Aerschot**
Supervisors: **Noémie Bidoul, Jean-Pierre Raskin**
Readers: **Denis Flandre, Loïc Lahaye, Jean-Pierre Raskin**
Academic year 2023–2024
Master [120] in Electrical Engineering

Abstract

Given the current climate crisis, it is crucial to rethink how production and consumption are approached, and this consideration applies to the electronics sector as well. An initial study has shown that the extraction and manufacturing processes involved in using gold for the metallic contacts in vanadium dioxide-based devices are the largest contributors to CO2 equivalent emissions. This research aims to evaluate the viability and characterize the use of aluminum as an alternative for these metallic contacts.

Vanadium dioxide is a particularly interesting material due to its reversible transition from an insulating to a metallic state at 68°C, which holds promise for numerous applications, including neuromorphic systems. Throughout this thesis, vanadium dioxide resistors are fabricated with aluminum contacts, using gold contacts as a reference. Each fabrication step is thoroughly explained. The devices are characterized using microscopy and Raman spectroscopy to ensure that the VO2 transitions correctly and to extract values for the VO2 sheet resistance as well as contact resistances with the different metals.

The study concludes by conducting aging tests to analyze the difference in aging between the two metals and to assess whether aluminum can serve as a sustainable and viable alternative to gold. The findings suggest that aluminum is indeed a potential alternative for these contacts, but significant variability was observed during measurements (both cycle-to-cycle and device-to-device variability). Additionally, a highly resistive first cycle was noted, indicating damage due to Joule heating, followed by a decrease in resistivity in subsequent cycles.

Acknowledgement

I would like to express my gratitude to those who actively contributed to the completion of this thesis through their knowledge, presence, and support.

First, I would like to thank my supervisor, Professor Jean-Pierre Raskin, who gave me the opportunity to work on this topic. His understanding and support have been very valuable throughout this journey.

A special thanks goes to Noémie Bidoul, whose constant presence from start to finish was crucial. Your guidance and assistance were not only instrumental in finalizing this project but also in navigating the challenges along the way. Your insights and encouragement provided me with the confidence to persevere, and I am deeply grateful for your dedication.

I would also like to express my appreciation to Pauline Raux, who began exploring this topic in her own thesis. Your analyses provided a strong foundation upon which I could build and develop my own work.

My sincere thanks to Sebastien Faniel for his guidance during the fabrication process at the WINFAB laboratory. Your expertise and patience were greatly appreciated.

I am also grateful to Nicolas André for answering my questions regarding the SEM and for being available whenever I needed assistance.

Thank you as well to Loïc Lahaye for guiding me through the lithography process.

I am also thankful to Denis Flandre, Christian Renaux, and David Bol for making themselves available to answer my questions when needed.

I would like to express my deepest gratitude to Julie Depauw for her moral support and assistance in proofreading this thesis.

Contents

List of Figures

List of Tables

Chapter 1

Introduction

In the 21st century, climate change has become a critical issue for our society. It refers to the gradual increase in the average temperatures of the Earth's atmosphere and oceans, primarily driven by human activities. This phenomenon has devastating consequences across various domains. The impacts are diverse and widespread, affecting all aspects of life on Earth. One direct outcome is climate disruption, leading to an increase in the frequency and severity of natural disasters such as extreme heatwaves, droughts, floods, and increasingly violent storms and hurricanes. Climate change also has a direct impact on biodiversity. Numerous species are losing their natural habitats, such as glaciers and polar ice caps, tropical forests, and coral reefs, resulting in the extinction of many species unable to adapt to such rapid changes. Droughts and disruptions in agricultural cycles can lead to food shortages. The degradation of climatic conditions, combined with the scarcity of natural resources, can lead to climate-induced migrations and escalate global tensions and conflicts. Climate change affects everyone without exception, and immediate actions are necessary to ensure the survival of humanity.

The causes of climate change are mainly the reduction of natural carbon sinks due to deforestation and the degradation of oceans, as well as the emission of greenhouse gases (GHGs). The sectors primarily responsible for these emissions include energy, agriculture, waste management, and industry. The electronics manufacturing sector, which continues to grow due to technological advancements, was responsible in 2021 for the production of 71.5 million tons of CO2 equivalent [43]. Additionally, the production of electronic waste is also on the rise and raises concerns. It is therefore necessary to consider reducing this production.

To address this, the first step is to quantify greenhouse gas emissions to identify the key sources of these emissions and the levers available to reduce them. A holistic method for quantifying this is Life Cycle Assessment (LCA). More and more companies are conducting LCAs. The LCA evaluates the environmental impacts of a product, service, or process throughout its entire life cycle. When conducting an LCA, it is important to define its goals and scope to properly analyze and interpret the data.

This thesis continues the work of another thesis conducted at UCLouvain in 2023 by Pauline Raux. This previous thesis presented the life cycle assessment of a microfabrica-

tion process for a vanadium dioxide-based device. The scope of this LCA was cradle to gate. This means that the LCA covered the process from the extraction of raw materials to the exit from the WINFAB laboratory. The objective was to identify hotspots and propose energy-efficient alternatives while also assessing the impact of these alternatives on device performance. The Primary Energy Demand (PED) in $[MJ/cm^2]$ was chosen as the indicator for the LCA. The most significant impact was observed during the metallization step, primarily due to gold deposition and its associated EI, representing 99.27% of the total PED. An alternative approach proposed replacing the gold metal layer with copper, resulting in a 99.25% reduction in the total PED [37]. Following this reduction in impact, a performance analysis was conducted, which demonstrated that copper exhibited some oxidation but remained a viable alternative to gold due to its performance. A proposed virtual process suggests substituting the gold deposit with aluminium, along with the utilization of different equipment, and replacing wet thermal oxidation with PECVD. The implementation of this virtual process results in a reduction of the total PED by 99.48%. A more in-depth analysis of this same process was later conducted and published by Noémie Bidoul, a PhD student at UCLouvain [2]. Indeed, obtaining the necessary data for Energy Intensity (EI) was very challenging and varied from one article to another. This ratio indicates the amount of energy required to produce one unit of mass of a product or material. The article confirmed that the use of gold for electrical contacts remains a critical step, albeit to a lesser extent, representing 38% and 49% of the total Cumulated Energy Demand (CED) and Global Warming Potential (GWP) associated with the device fabrication. The article also stated that replacing gold with aluminium as a way to curb the total process CED and GWP by 25% and 43%, respectively.

The objective of this thesis is therefore to identify and analyze a potential alternative to gold contacts. The use of gold is responsible for the largest CED and GWP in the process for VO2-based devices. This thesis begins by describing the intrinsic functioning of VO2, its applications, and the associated damage and variability. We also discuss the contact resistivity with the metals used for connections. We then explain our choice of metal, which fell on aluminium. The subsequent sections describe each step of the fabrication process in section 4. We fabricate VO2 devices with gold and aluminium contacts. After fabrication, we begin the characterization of the devices through microscopic observation and Raman spectroscopy. We then ensure that the devices exhibit a transition and characterize the sheet resistance and contact resistance of the devices for both metals used. Finally, we investigate the difference in aging of the devices under DC and AC regimes for the two metals used for the contacts. The thesis concludes with a final summary.

Chapter 2

State of the art

2.1 Vanadium dioxide VO_2

2.1.1 T-IMT in vanadium oxides

Certain materials possess the remarkable ability to transition between a metallic and an insulating state when subjected to external stimuli. These materials, known as Insulator-to-Metal Transition (IMT) materials, exhibit a distinctive characteristic wherein their resistivity undergoes a sudden and reversible change upon reaching a specific critical temperature, a phenomenon identified as the thermal IMT (T-IMT).

Among these IMT materials, vanadium oxides have garnered significant attention due to their strong electron correlations and the potential applications arising from their IMT properties. Within the various stoichiometries of vanadium oxides, V2O3, VO2, and V2O5 stand out as the most extensively researched compounds.Vanadium pentoxide (V2O5), characterized by the highest oxidation state of vanadium oxides, is the most stable compound within this family. Although V2O5 does not exhibit an IMT transition, it remains a subject of intense research due to its promising electrochromic applications. In contrast, V2O3 is notable for its well-defined Mott phase transition, which occurs at a temperature around 150 K. This transition is of particular interest in studies focusing on Mott insulators, where electron-electron interactions play a pivotal role in the phase change.[12]

Vanadium dioxide (VO2) has garnered significant attention because of its insulator-to-metal phase transition that occurs close to room temperature, rendering it applicable for innovative electronic technologies. This phase transition, wherein VO2 shifts from an insulating to a metallic phase, occurs at a critical temperature of approximately 68°C (341 K) and is marked by a dramatic decrease in resistivity by several orders of magnitude. Additionally, the metal-to-insulator (MIT) phase transition takes place at a slightly lower temperature than the critical temperature, leading to a thermal hysteresis cycle that we

can observe in figure 2.1.

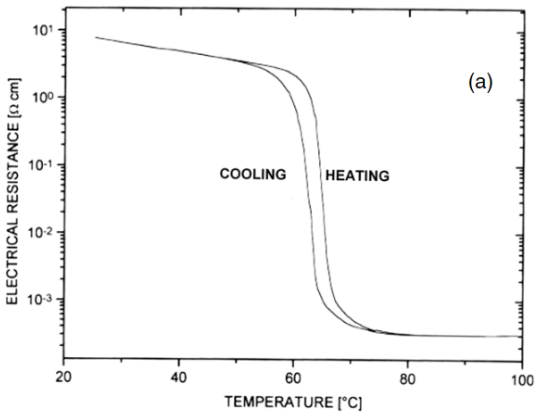

Figure 2.1: Thermal hysteresis curve of vanadium dioxide [32]

At room temperature, VO2 exhibits a monoclinic (M1) crystal structure and semiconducting properties. However, when the temperature exceeds 340 K, VO2 undergoes a structural transition to a tetragonal, rutile crystal structure. A crucial aspect of VO2 is that its transition temperature can be adjusted through doping. The introduction of atoms such as iron or cobalt lowers the transition temperature, while the incorporation of germanium raises it. This tunability of T_c can be highly advantageous depending on the specific application intended for the material.

The exact nature of the phase transition in VO2 continues to be a topic of debate among researchers. Numerous studies suggest that the transition results from the combined effects of two interrelated mechanisms that cannot be fully disentangled. The first mechanism is the Mott transition, a process where a material shifts from an insulator to a conductor due to electron-electron interactions rather than mere changes in temperature or pressure. In Mott insulators, strong repulsive forces between electrons inhibit their free movement, maintaining the material in an insulating state. However, under certain conditions such as increased pressure or doping, these interactions can be overcome, resulting in a sudden transition to a metallic state. The second mechanism involves the Peierls instability, which occurs in one-dimensional materials where a uniform atomic arrangement becomes unstable at low temperatures. This instability causes a spontaneous distortion of the atomic lattice, leading to the opening of a gap at the Fermi level and transitioning the material from a metallic to an insulating state. The resulting lattice distortion lowers the system's overall energy, stabilizing the material in this new, lower-energy configuration. The Peierls instability is thought to be responsible for the structural reconfiguration observed during the phase transition in VO2.[12]

2.1.2 E-IMT

While thermal IMT is a primary method of inducing the transition in VO2 by modulating its temperature, other stimuli can also trigger this transformation. Strain, optical activation, and electrical activation (E-IMT) are alternative mechanisms that can achieve the same transition, thereby expanding the potential applications of VO2 and other IMT

materials in advanced technologies.

In this thesis, particular attention will be given to the transition induced by electrical activation. The E-IMT (Electric-Field Induced Metal-Insulator Transition) offers promising prospects for applications such as neuromorphic circuits, which will be further explored in section 2.1.3.

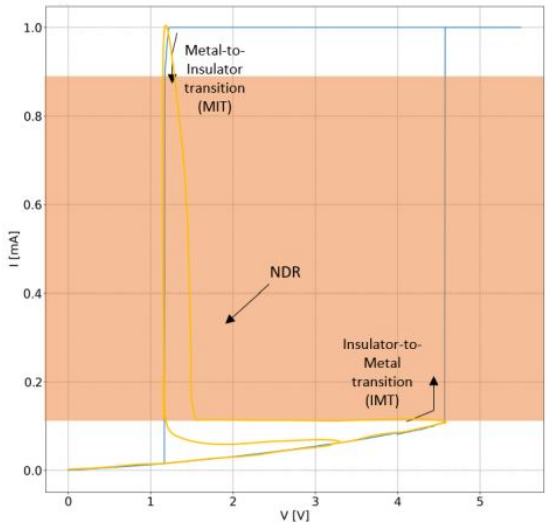

Figure 2.2: I-V characteristic curves of the transition in a VO2 device. The yellow curve is current-controlled, while the blue curve is voltage-controlled. [37]

The I-V characteristic curves of vanadium dioxide (VO2) devices can be observed in Figure 2.2. The blue curve represents a voltage-controlled I-V curve, while the yellow curve represents a current-controlled I-V curve. On the voltage-controlled curve, a sharp increase in current is observed beyond a certain voltage threshold V_{TH}, indicating a change in resistivity and thus the transition of the device. It is noted that at a certain point, the current ceases to increase and plateaus. This plateau is due to a predefined maximum current limit set by the equipment to protect both the devices and the equipment from potentially damaging high currents. Additionally, the curve exhibits hysteresis, and the voltage at which the current sharply decreases V_{TL}, signaling the transition back to the insulating phase, is lower than V_{TH}. When V_{TH} is reached under current control (yellow curve), a region of negative differential resistance (NDR) is observed. This region is characterized by a decrease in the voltage across the VO2 as the current increases, which is particularly interesting for operating devices in a spiking regime, as described in section 5.4.

It is well established that the phase transition within a device does not occur uniformly but rather progresses through the formation of filaments. At the transition voltage V_{TH}, the first VO2 grains transition and become metallic. Subsequently, adjacent grains, experiencing an increase in the electric field, also transition, forming a metallic filament between the two electrodes, thereby causing a drop in resistivity. This filament exhibits a very high current density, generating significant heat due to the Joule effect [4]. If the voltage or injected current continues to increase, the heat rises, causing adjacent grains near the filament to transition, thereby enlarging the metallic filament [41].

However, similar to the thermal insulator-to-metal transition (T-IMT), the precise nature of the electronic insulator-to-metal transition (E-IMT) remains ambiguous. Numerous studies advocate the hypothesis that the transition is primarily driven by the Joule effect. In this context, as electrons, which serve as charge carriers, traverse a conductor, they encounter resistance due to collisions with the atoms in the material. These collisions result in the dissipation of energy as heat. Consequently, as the applied voltage increases, the current correspondingly rises, leading to a temperature increase that eventually reaches the critical transition temperature T_c.

On the other hand, some research suggests that the heat generated by the Joule effect may not be sufficient to attain the critical temperature necessary for the transition. Instead, these studies propose that the transition might be triggered by the injection of charge carriers. This ongoing debate underscores the complexity of the mechanisms at play in E-IMT and highlights the need for further investigation to fully understand the interplay of thermal and electronic factors involved in this process. Such insights are crucial for advancing the development of devices that exploit this transition for practical applications. [12]

2.1.3 Applications

The phase transition in VO2 significantly impacts not only its electrical resistance but also its optical and thermal properties, enabling VO2 to have a wide range of applications. One of the major applications of VO2 is in neuromorphic systems, briefly described below.

Neuromorphic Systems

In recent years, with the development of the Internet of Things (IoT), there has been an explosion in the amount of data generated and collected. The acquisition and processing of this data require substantial computational power and memory, leading to high energy consumption. Moreover, data transfers between the processing unit and memory limit data processing speed. Consequently, the scientific community is working to improve data acquisition and processing systems by designing highly parallel, interconnected, and reconfigurable systems that eliminate the separation between memory and processing units [12].

In response to these challenges, a promising approach involves rethinking the architecture of computing systems and sensors by drawing inspiration from the human brain's functioning. The human brain processes information efficiently by converting it into electrical impulses. The term "neuromorphic" refers to the design of circuits and systems that mimic the neural architecture of the human brain.

An example of a neuromorphic system is Spiking Neural Networks (SNNs). This method of neuromorphic computing is considered a neuromorphic alternative to traditional neural network architectures, such as Convolutional Neural Networks (CNNs). Unlike traditional neural networks that use continuous values, SNNs communicate via electrical impulses or "spikes." In these networks, a neuron sends a spike to its neighbors only when a certain threshold is reached. They are more energy-efficient and potentially more powerful for real-time information processing. These neural networks are widely used in deep learning, a rapidly growing branch of artificial intelligence with significant applications in areas such as facial recognition, autonomous driving, and disease detection in medical imaging.

Additionally, inspiration can be drawn from human receptors to create neuromorphic sensors. In traditional architectures, analog data collected by sensors are first converted into digital signals using Analog-to-Digital Converters (ADCs), then stored in memory before being sent to processing units. This process leads to high energy consumption and low efficiency. In contrast, human receptors convert physical information into electrical impulses, which are then transmitted to the cerebral cortex. To create a system resembling human receptors, it is necessary to combine sensors with artificial synapses and neurons [47].

Traditional CMOS technologies are inefficient for building these neuromorphic structures. However, VO2-based devices still require extensive research on damage and variability before they can be fully exploited.

2.1.4 Variability

Cycle-to-cycle and device-to-device variations

To better implement these applications, it is crucial to precisely understand the characteristics of VO2, such as its resistivity in both phases and its transition voltage V_{TH}. However, when cycling two-terminal devices in voltage or current, it is observed that the characteristics of VO2 exhibit cycle-to-cycle variations. As explained in section 2.1.2, the phase transition does not occur uniformly within the devices but rather involves certain grains that form filaments in the vanadium dioxide, allowing current to pass. Among the grains that have transitioned, some may remain in their metallic phase for several milliseconds after the current is turned off. These grains become preferential sites for current passage, increasing the probability that the next metallic filament will form through them. There are multiple paths through which current prefers to flow, leading to variations in device characteristics from one filament to another and consequently from one cycle to another [4][3]. Moreover, it has been shown that in the presence of these remanent metallic domains after a cycle, the probability that VO2 transitions at a lower voltage than the characteristic V_{TH} is not negligible [42]. Another mechanism potentially responsible for these variations is the fact that some grains may change their crystalline orientation from one cycle to the next [3]. For devices that spike VO2 at a certain frequency, such as oscillators, this induces jitter. The crystalline quality of epitaxially grown VO2 significantly influences cycle-to-cycle variations. Achieving high crystalline quality in epitaxial VO2 can substantially reduce these variations, thereby enhancing the uniformity of VO2-based devices [47].

Device-to-device variation is generally reported to be higher than cycle-to-cycle variation [18][47]. These variations arise from differences in the VO2 layer's structure between devices. To mitigate this impact, it is essential to achieve high-quality VO2, characterized by a minimal number of impurities and crystal defects, to ensure the highest possible uniformity of the VO2 layer. Calibrated resistors and coupled capacitors are discussed in the literature as methods to mitigate device-to-device variability in circuits employing VO2 resistors [45][47].

Impact of the Grains

It is well established that grain size impacts the transition characteristics of vanadium dioxide. The grain size is primarily determined by the annealing temperature [27][26][3]. Indeed, higher temperatures promote diffusion and increase grain size. Devices with smaller grains exhibit lower insulating resistance, transition voltage V_{TH}, transition temperature, and OFF/ON resistivity ratios. They also present a wider hysteresis 2.3. This may be due to oxygen-deficient stoichiometry in VO2 and a higher concentration of crystalline defects [3].

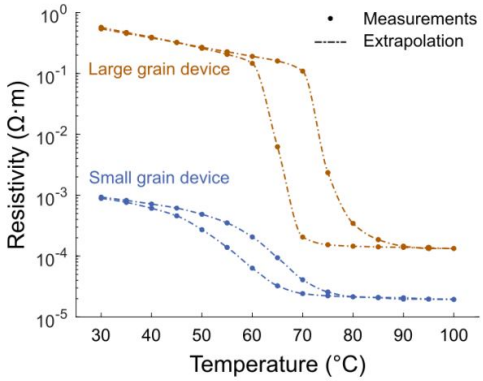

Figure 2.3: Impact of the grain size on the hysteresis curve of vanadium dioxide [3]

Additionally, the larger the grains compared to the dimensions of the device, the greater the cycle-to-cycle variations in the insulating phase resistance and the transition voltage V_{TH} [3].

2.2 Metal contact

Here are some concepts that are crucial for understanding the selection of metals used for the connections in devices.

2.2.1 Contact resistivity

Contact resistance is a critical factor in the performance and reliability of electrical and electronic devices, particularly in microelectronics where it plays a significant role in determining the efficiency and functionality of circuits. The contact resistance refers to the resistance encountered at the interface between two conductive materials, often at a metal-semiconductor or metal-metal junction. [44][9]

This resistance can significantly impact the overall resistance of a circuit, especially in devices with small-scale geometries where contact areas are minimal. Low contact resistance is desirable because it ensures efficient current flow between the contacts, leading to better device performance.

High contact resistance, on the other hand, can lead to power losses, heat generation, and potential failure of the device. It can also cause signal distortion, affecting the accuracy and speed of electronic components. Therefore, minimizing contact resistance is crucial in the design and fabrication of electronic devices.

In semiconductor microfabrication, ensuring Ohmic contacts is equally crucial. An Ohmic contact is a type of connection between a metal and a semiconductor where the electrical resistance remains constant, regardless of the applied bias (i.e., the current passing through the contact). This type of contact behaves like a pure resistor, with no rectifying effect, meaning that the current flows equally well in both directions, in accordance with Ohm's law [11].

This is essential for ensuring efficient current transmission between a metal and a semiconductor without introducing undesirable nonlinearities that could, in our case, alter the characteristics of the VO2 transition and the operation of the devices.

Ohmic contacts is dependent on the Schottky barrier. When a metal and a semiconductor are brought into contact, electrons will flow from the material with a lower work function (the minimum energy required to move an electron from inside the material to just outside its surface) to the one with a higher work function until the Fermi levels of the two materials align. This movement of electrons creates a region at the interface where charge accumulates, resulting in an electric field and a potential energy barrier known as the Schottky barrier. The Schottky barrier height determines how easily electrons can move from the metal to the semiconductor or vice versa. If the Schottky barrier height is significant, the contact will exhibit rectifying behavior, meaning it allows current to flow easily in one direction (forward bias) but not in the opposite direction (reverse bias). If the Schottky barrier is low or negligible, or if the semiconductor is heavily doped, the contact will behave as an ohmic contact, allowing current to flow equally well in both directions, with little resistance. [10]

The Schottky–Mott rule predicts the height of the Schottky barrier based on the work function of the metal and the semiconductor. Thanks to this rule the conditions to have

an ohmic contact becomes [24]:

For n-type semiconductors:

$$\phi_{\text{metal}} < \phi_{\text{s}} \tag{2.1}$$

For p-type semiconductors:

$$\phi_{\text{metal}} > \phi_{\text{s}} \tag{2.2}$$

ϕ_{metal} and ϕ_{s} are the works function of the metal and the semiconductor. is the least amount of energy required to extract an electron from the surface of a material and transfer it to a point just outside the material.

However, the Schottky–Mott model was found to be inaccurate due to the phenomenon of "Fermi level pinning," where certain energy states in the semiconductor's band gap become locked to the Fermi level. Therefore, predictions with work function provide initial guidance, but practical considerations such as Fermi level pinning and doping must be taken into account, often necessitating experimental validation.

Chapter 3

Choice of metal for connections

Before proceeding with device fabrication, it was necessary to decide on the contact metals to be studied in order to find a viable alternative to gold. The first metal to be deposited would be gold, serving as a reference for subsequent comparison of the devices. aluminium was chosen as the second metal, as proposed in the previous work on this subject [37]. The reasoning behind this choice is detailed in the following sections of this chapter.

The selection of the metal was carried out in several stages. The first step involved choosing a metal that was on the list of depositable metals in the Winfab cleanroom.

Next, to be of real interest, this metal needed to have a significantly lower energy intensity than gold. Energy intensity (EI) represents the amount of energy required to produce one unit of mass of a product or material. This indicator is very high for gold, at 208,000 MJ/kg, due to the rarity of this element on Earth. In contrast, the EI of aluminium is three orders of magnitude lower, at 131 MJ/kg [36].

The third step was to select a metal with resistivity several orders of magnitude lower than the resistivity of the metal in both the insulating and metallic regimes. aluminium has a resistivity of $2.8210^{-8}\Omega * m$, compared to $2.4410^{-8}\Omega * m$ for gold [1]. Another important characteristic to consider is the contact resistance (see section 2.2). Indeed, to avoid non-idealities and effects due to the Schottky barrier and to maintain a linear contact resistance (Ohmic contact), attention must be paid to the work function of the metal. This value provides an indication of the type of contact expected from a junction, although it does not guarantee it. By averaging the values found in the literature, a work function of $\phi_{V_{VO2}} = 5.12eV$ for vanadium dioxide [37], $\phi_{V_{Au}} = 4.95eV$ for gold [37], and $\phi_{V_{Al}} = 4.2eV$ for aluminium [31][8][25] was obtained. The work functions of the two metals are close to that of VO2. Moreover, since VO2 is intrinsic, and both gold and aluminium have a slightly lower work function than VO2, this results in an Ohmic contact for electrons.

Another consideration was the oxidation of the metal. The oxidation of the metal over time and the presence of water vapor in the atmosphere results in a deterioration of its resistance and contact resistance over time. aluminium oxidizes over time but forms a

protective oxide layer on the surface, preventing further oxidation of the aluminium.

An equally important criterion was that the metal be CMOS-compatible. Indeed, these devices are generally placed with transistors in applications to be able to put VO2 in an unstable state where it alternates between its two states. For this purpose, the metal used for contacts during the VO2 device processing must be CMOS-compatible. The issue with gold, in addition to its high EI and cost, is that it is not CMOS-compatible, whereas aluminium is. aluminium is typically slightly doped with a few percentages of silicon to avoid the need for a TiN barrier or others.

Finally, the article [5] presents a holistic sustainability assessment framework for evaluating alternative metals for advanced applications. This article compares different metals across various aspects. The evaluated criteria are: Supply Risk, Criticality and Conflict, Circularity, Impact on Climate Change, Water Use, Impact on Natural Resources, and Impact on Human Health. This study positions aluminium as one of the best metals for these criteria. It performs poorly in only two criteria. The first is supply risk, as the aluminium market is not considered competitive enough. The second criterion is Criticality and Conflict, highlighting that its availability is crucial for national security or economic growth.

Considering all these criteria, aluminium appeared to be the best candidate.

Chapter 4

Fabrication

In order to characterize and investigate the differences between VO2-based devices with gold contacts and those with Aluminium contacts, various devices were fabricated in the cleanroom at UCLouvain through Winfab. Winfab operates as a multidisciplinary platform across several research and technological fields. Its aim is to support students and researchers in their work and to collaborate with certain industries. Winfab boasts a cleanroom equipped with numerous machines dedicated to microfabrication. This cleanroom is accessible through airlocks, requiring personnel to wear protective suits, and is equipped with facilities for air-conditioning, water, and chemical delivery. Contamination of wafers by impurities of any kind can affect the behavior and even the functionality of the fabricated devices. This cleanroom is primarily dedicated to research and is not optimized for the industrialization of a particular device. This means that the equipment does not have large capacities to accommodate many wafers simultaneously. Additionally, the equipment must be shared by numerous students and researchers for entirely different processes, which significantly reduces equipment availability and increases the probability of cross-contamination between different processes. However, the research-focused nature of this cleanroom also allows for great freedom in what can be investigated and the equipment that can be utilized.

The devices intended for studying the behavior of vanadium dioxide and the impact of contacts are VO2 resistors. As reported in the literature review, when the V02 transitions from an insulating to a metallic state the resistivity decreases sharply. Consequently, numerous resistors with varying lengths and widths have been fabricated on each wafer. What is referred to as a device in this thesis are VO2 two-terminal devices, consisting of two metal contacts deposited on a vanadium oxide layer. The current flows through one of the metal contacts, passes through the VO2 channel, and exits through the other contact. The fabricated devices are illustrated in the image 4.1. A zoom-in on the VO2 channel of one of the devices 4.2 is provided to better visualize the channel length L and its width W. The size of the contacts (the pentagons in the image 4.1) is significantly larger than the channels. Specifically, the contacts have a size of 150x150 µm (excluding the tips of the pentagons, as these vary depending on the width of the channel) compared to the channels, which have a length ranging from 0.6 µm to 6 µm. A larger contact area helps

reduce contact resistance.[6] [29]

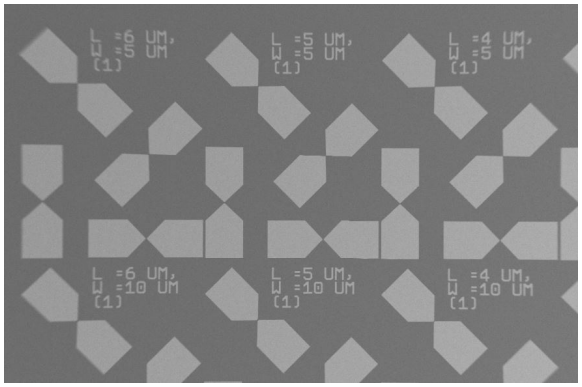

Figure 4.1: SEM image of various two-terminal devices with gold contact

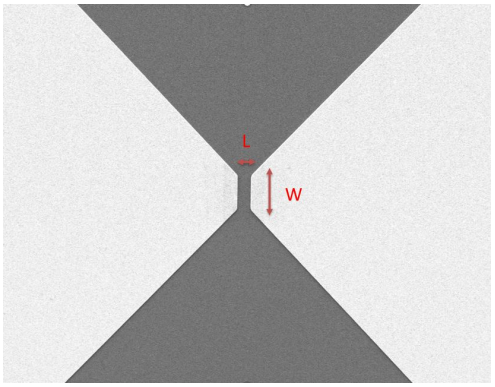

Figure 4.2: Zoom on a channel of a two-terminal device with gold contact and L[um]=2 and W[um]=5

The process involves depositing a layer of VO2 on the wafers and subsequently depositing the metal contacts. This chapter details each fabrication step, explaining the working principles and the parameters applied to our process. The procedure begins with a standard cleaning of the wafers followed by wet thermal oxidation. Subsequently, sputtering is employed to deposit vanadium dioxide. To accurately place the contacts, photolithography is performed before proceeding to metallization. Finally, the residual photoresist layer and the metal on top are removed through a lift-off process. These steps and their significant parameters are detailed in the table below. A cross section of the wafer at each fabrication step and a final top view is represented in Figure 4.3

Summarized process sheet		
Fabrication step	**Equipments**	**Thickness[nm]**
1. Standard cleaning	Wet benches	/
2. Wet Thermal oxidation	Koyo Furnace	400
3. Sputtering	AJA	190
4. Annealing	furnace	/
5. Photolithography	LP-III oven SUSS Gamma SUSS MA6	/
6. Metalization	Vacotec and VST	150
7. Lift off	wet bench	/

Table 4.1: Summarized process sheet for the fabrication of the devices

In this work, six wafers were used for fabrication, aiming to deposit three different metals to study their impact on device behavior. Gold was deposited on the first two wafers to serve as a reference for comparison with the other metals. Aluminium was deposited on the next two wafers. No metal was deposited on the final two wafers, allowing for

the possibility of testing another metal later if time permitted. Unfortunately, this was not possible. Two wafers were designated for each metal to provide a backup in case of fabrication defects on one wafer.

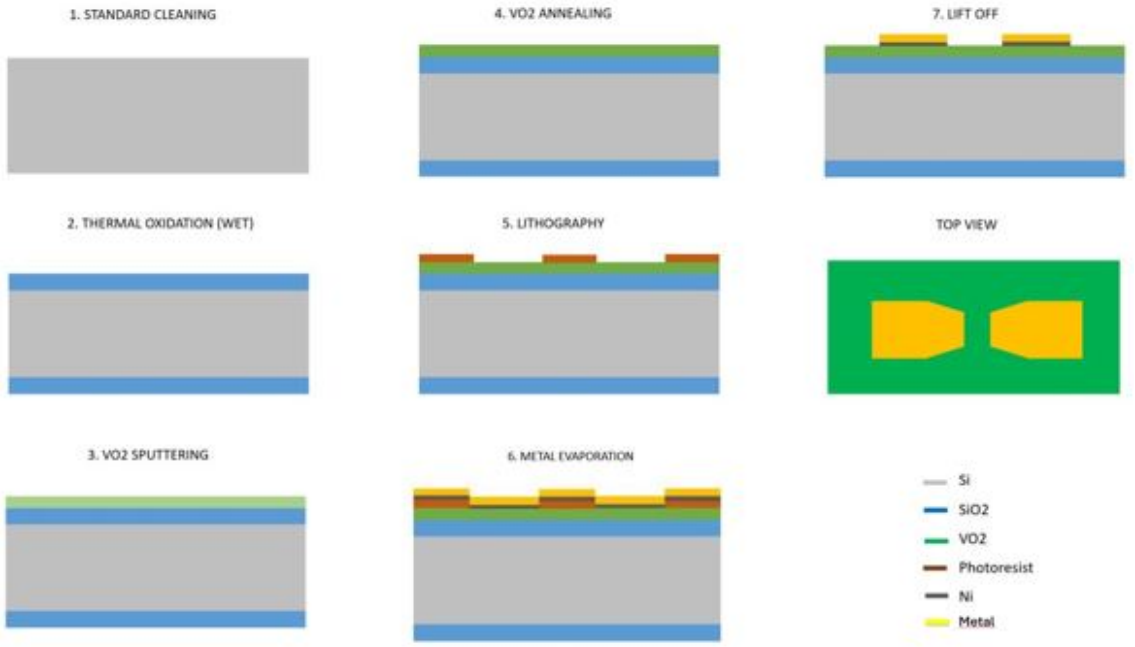

Figure 4.3: Cross section and final top view of the microfabrication process of VO2 device [37]

4.1 Standard cleaning

4.1.1 Pinciple

The first step for almost every micro-fabrication process is the standard cleaning. This involves soaking the wafers in several baths of acid to remove any impurities that may have settled on the silicon wafers, as well as the native oxide layer. These baths can also be heated to the desired temperature if a specific chemical reaction requires it. At the end of the standard cleaning process, the wafers are dried and ready for the subsequent fabrication steps. This step is crucial to avoid any contamination, as even the slightest impurity or contamination could affect the quality or functionality of the devices.

4.1.2 Process

Within the process, the wafers are successively immersed in a piranha solution bath for 10 minutes at 110°C. This solution consists of a mix of H2SO4 and H2O2.

The reaction between these two acids is exothermic, naturally producing heat. However, additional energy in the form of heat is supplied to maintain a constant bath temperature of 110°C, preventing temperature fluctuations as the reaction progresses. The purpose of this bath is to eliminate organic compounds that may have deposited on the surface of the silicon wafers.

Subsequently, the wafers are rinsed in deionized water baths at 25°C for 10 minutes. Nitrogen, an inert gas, is injected into these baths to create agitation, enhancing the rinsing process. The water is changed five times during this period to remove any remaining chemical residues (H2SO4, H2O2, HF). These two baths are repeated for added security to ensure all impurities are thoroughly removed.

The baths are located in "wet benches," which feature hoods to prevent users from inhaling gases and glass shields to protect against acid or other liquid splashes.

Afterward, the silicon wafers are immersed in 2% hydrofluoric acid at 25°C for 15 seconds to remove the native SiO2 oxide layer on the surface (a few angstroms thick). Finally, the wafers are dipped in deionized water one last time before being dried in a rinser-dryer, a centrifuge, for 4 minutes at 880 rotations per minute.

Standard cleaning		
Parameters	**Bath 1 & 2**	**Bath 3**
Equipment	wet bench	wet bench
Composition	H_20_2 and H_2SO_4	HF 2%
Temperature [K]	383.15	298.15
Duration [s]	600	15

Table 4.2: Parameters of standard cleaning

4.2 Wet thermal oxidation

To study the behavior of vanadium dioxide without interaction with silicon, an insulating layer must be employed to separate them. Additionally, due to the different crystal lattices of VO2 and silicon, crystallizing vanadium dioxide on an amorphous layer such as SiO2 is more feasible in terms of tensile stress[46]. This is achieved by oxidizing the silicon surface in a furnace to create a SiO2 layer between the silicon and VO2.

4.2.1 Principle

The silicon wafer is placed in a high-temperature furnace with a controlled steam flow to promote oxidation. Under the influence of heat and steam, oxygen bonds with the silicon, forming a surface layer of silicon dioxide.

$$Si + 2H_20 \longrightarrow Si0_2 + 2H_2 \tag{4.1}$$

This reaction is known as wet thermal oxidation.[19] The oxidation rate depends on the temperature, the partial pressure of steam, and the crystalline orientation of the wafer. As long as the wafer remains in the high-temperature furnace under gas flow, oxygen continues to diffuse through the silicon dioxide layer and bond with the silicon, thereby enlarging the oxide layer (SiO2) and consuming the remaining silicon. The growth rate typically follows the Deal-Grove diffusion law. Once the desired thickness of the silicon dioxide layer is achieved, the silicon wafer is cooled, removed from the furnace, and prepared for subsequent fabrication steps.

4.2.2 Process

In this process, after placing the wafers in the Koyo furnace, the temperature reaches 1000°C. Oxygen (O2) and hydrogen (H2) are injected into the furnace, combining to form water vapor (H2O) to initiate wet thermal oxidation and create the SiO2 layer. Nitrogen is also introduced as an inert gas to regulate pressure. The process lasts 3 hours and 4 minutes to achieve a 400 nm silicon dioxide layer, and it comprises 16 steps involving variations in temperature, gas composition, and pressure.

Parameters	**Wet thermal oxidation**
Equipment	Koyo furnace
Input gazes	0_2 & H_2 & N_2
Thickness of the layer [nm]	400
Duration [min]	184

Table 4.3: Parameters of wet thermal oxidation

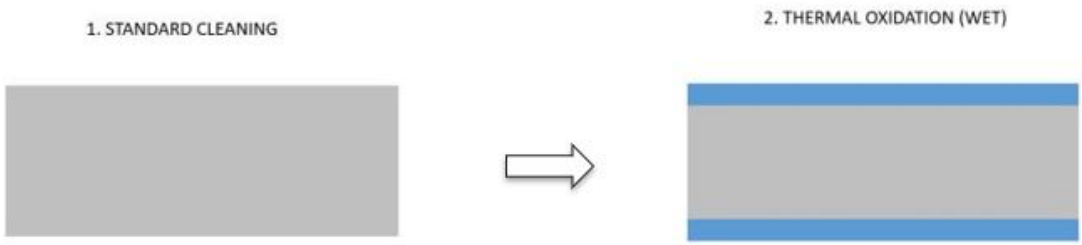

Figure 4.4: Cross section of the wet thermal oxidation microfabrication step [37]. The color gray represents Si, while blue represents SiO2.

4.3 VO2 sputtering

With the silicon isolated by the oxide layer, it is now possible to deposit vanadium dioxide (VO2). This deposition is achieved on the wafer using a physical vapor deposition technique known as sputtering.

4.3.1 Principle

The principle of sputtering involves bombarding a sample of the desired material with ions, causing atoms of the material to be ejected onto the substrate. The deposition chamber is maintained under vacuum and contains a thick disk of the target material, referred to as the target. At both ends of the chamber are electrodes that together create an electric field. The wafer is placed in the deposition chamber above the target and between the electrodes.

An inert gas, argon, is introduced into the chamber and ionized by the electric field produced by the electrodes, creating a plasma. The ions from the plasma (Ar+) are attracted to the cathode and accelerated by the electric field before colliding with the target in front of the cathode. This collision results in a transfer of momentum between the argon ions and the atoms of the target, causing the target atoms to be ejected and deposited as a thin layer on the wafer above the target.

Several parameters influence the thickness and quality of the deposited layer, such as the duration of deposition, pressure, distance between the cathode and the substrate, and the power of the electric field. Additionally, a continuous or alternating field can be used, with an alternating field being beneficial for maintaining the plasma when using an insulating target material.

Another important parameter is the gas introduced during deposition. By injecting gases other than argon (such as oxygen, nitrogen, or carbon), the ejected target particles can react with the introduced gases to form more complex compounds on the substrate. This process is known as reactive sputtering.

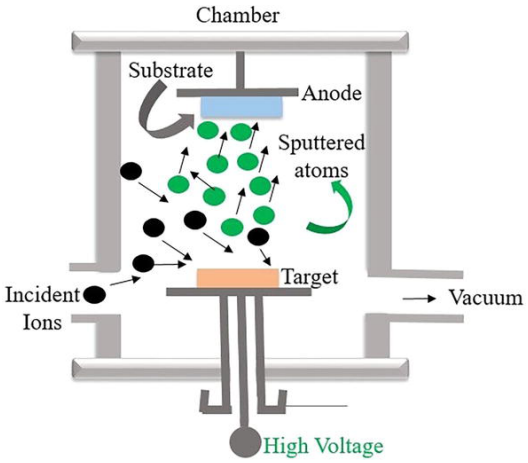

Figure 4.5: Sputtering principle [15]

4.3.2 Process

In this process, the target used is a vanadium target with a thickness of 6.35 mm and a diameter of 50.8 mm. The equipment employed for sputtering is the AJA system, which includes both a loading chamber and a deposition chamber. The loading chamber, equipped with primary and turbo pumps, initially reduces the pressure when inserting the wafer, thereby maintaining the vacuum in the deposition chamber during each deposition cycle.

Reactive sputtering is utilized, involving the introduction of oxygen in addition to argon into the chamber during deposition. This ensures that the vanadium atoms ejected from the target bind with the oxygen, resulting in the formation of vanadium dioxide on the wafer surface. The partial pressure of oxygen in the deposition chamber is a critical factor that determines the stoichiometry of the thin deposited layer and, to a lesser extent, the grain size.

It has been demonstrated that VO2 can be obtained by selecting an oxygen partial pressure of 13% on this equipment. Additionally, Raman spectroscopy has revealed the presence of other vanadium and oxygen stoichiometries at higher oxygen partial pressures during sputtering. Finally, this partial pressure results in relatively small VO2 grains after annealing.[3]

The following table summarizes the various parameters involved in the sputtering process:

Parameters	**Sputtering**
Equipment	AJA
Target	Vanadium
Input gazes	0_2(13%/6.5sccm) & Ar(87%/43.5sccm)
Chamber pressure during sputtering [mTorr]	5
Plasma Power [W]	200
Thickness of the layer [nm]	190
Duration [min]	23

Table 4.4: Parameters of sputtering

It should be noted that before each exposure of the wafers to the target, the target was bombarded with argon for 5 minutes to remove any surface layer that might have been contaminated by previous processes. The AJA system contains multiple targets of different materials, necessitating this cleaning step. This initial stage is followed by an additional 5 minutes of oxygen introduction (at 13% partial pressure) to ensure homogeneity of the gas in the chamber. After these 10 minutes, the shield protecting the wafer above the target is removed, and the 23-minute deposition begins.

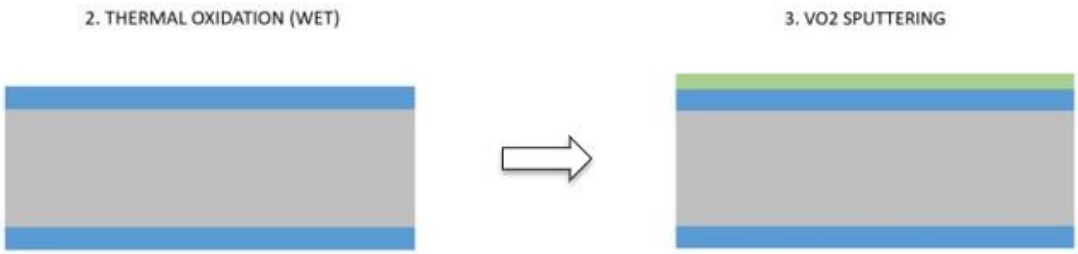

Figure 4.6: Cross section of the sputtering microfabrication step [37]. The color gray represents Si, while blue represents SiO2 and green VO2.

4.4 Annealing

Following sputtering, the deposited vanadium dioxide layer is amorphous, meaning the atomic structure lacks order. During the phase transition, current filaments form, generating significant heat within these filaments, which in turn crystallizes the grains within them. This process results in a non-uniform VO2 layer, introducing greater variability in the electrical characteristics of the material. To mitigate this, annealing is performed to achieve a polycrystalline VO2 layer.

4.4.1 Principle

The wafers are placed in a furnace, and the pressure is reduced. The temperature is then increased to the desired level and maintained for a predetermined period. Finally, the furnace is cooled down to ambient temperature. The time, annealing temperature, and heating rate are determined based on the required specifications. These parameters significantly influence the grain size of the VO2 layer, which in turn affects the electrical characteristics of VO2, such as its resistance in both states and its transition temperature.

Figure 4.7: Photo of our furnace in Winfab cleanroom, the horizontal tubular chamber

4.4.2 Process

The wafers are placed in a horizontal tubular chamber (image 4.7) dedicated primarily to processing wafers containing VO2, thereby minimizing contamination during this step. The pressure is reduced to 20 mTorr using a pump. Subsequently, a flow of argon gas (30 sccm) is introduced into the chamber to purge any impurities, raising the pressure to 165 mTorr. This argon flow is maintained throughout the annealing process. The chamber is then heated, taking 30 minutes to reach the target temperature of 500°C. This temperature facilitates crystallization while remaining relatively low, thereby producing small grains. This temperature is maintained for 1

hour, followed by an additional hour required for cooling to ambient temperature (approximately 25°C in the cleanroom). The chamber is heated by an external resistor controlled by a PID regulator (closed-loop system).

Parameters	**Annealing**
Equipment	annealing oven
Input gazes	Ar (30 sccm)
Furnace pressure [mTorr]	165
Temperature [K]	773.15
Total duration [min]	150

Table 4.5: Parameters of annealing

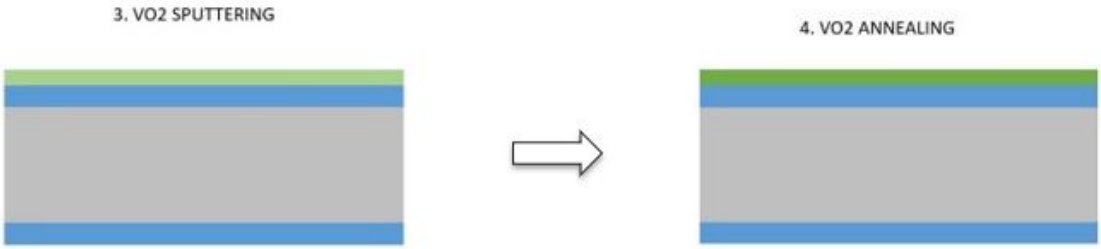

Figure 4.8: Cross section of the annealing microfabrication step [37]. The color gray represents Si, while blue represents SiO2 and green, crystallized VO2.

4.5 Photolithography

With the VO2 crystallized, the next step is to place the metallic contacts. To accurately position these contacts, photolithography is employed.

4.5.1 Principle

Photolithography allows the transfer of a pattern onto a wafer using light. The first step in performing lithography is to apply a layer of photosensitive resin (photoresist). There are two types of photoresist: positive and negative. Positive photoresists become soluble in a developer after exposure to ultraviolet (UV) light, whereas negative photoresists exhibit the opposite behavior, with only the non-exposed areas being soluble in the developer. Typically, the photoresist is applied by spin-coating, a process in which liquid resin is dispensed onto the wafer while it rotates at high speed. This rotation spreads the resin evenly across the wafer, creating a uniform layer of consistent thickness due to the centripetal force.

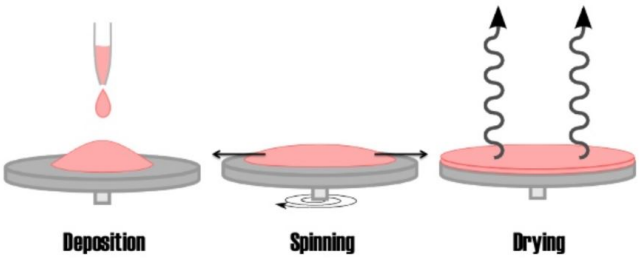

Figure 4.9: Principle of spin coating [14]

Next, the mask with the desired pattern is placed above the wafer, and they are exposed to light. The wavelength of the light affects the resolution of the pattern on the wafer. The exposed photoresist (positive/negative) undergoes a chemical reaction (molecular chain breaking/chain strengthening) caused by the light, rendering it soluble/insoluble in the developer.
Finally, the wafer is immersed in a developer solution, dissolving the exposed positive photoresist or the unexposed negative photoresist. Consequently, the pattern of the remaining photoresist on the wafer serves as a mask for subsequent fabrication steps.

4.5.2 Process

As part of the process, the wafers are initially heated to 100°C in an LP-III furnace for approximately 23 minutes to eliminate any residual moisture, which could otherwise diminish the adhesion between the photoresist and the substrate. During this time, a gaseous adhesion promoter, Hexamethyl disilazane (HMDS), is introduced into the chamber to treat the wafers, thereby enhancing the adhesion of the photoresist during the coating process. Strong adhesion is crucial for minimizing defects such as bubbles, delamination, or variations in the photoresist thickness, and it also improves the lithographic resolution, allowing for more precise definition of patterns, especially when they are intricate or fine.

Subsequently, the wafers are transferred to the SUSS Gamma, an automated machine equipped with a robotic arm that handles spin coating, baking, and developing of the wafers one by one. A thin layer of AZnLof5510 photoresist is applied to each wafer, with 3 ml of photoresist dispensed while the wafers spin at 3000 rpm for 60 seconds.

Following this step, the wafers undergo a 60-second bake at 90°C to dry the photoresist.

While the SUSS Gamma manages the spin coating and baking, the mask, previously designed within the lab prior to this work, is cleaned using acetone, methanol, and deionized water, followed by drying with a nitrogen gun.

Once the wafers have been baked and the mask cleaned, the wafers are individually exposed to ultraviolet light through the mask using the SUSS MA6 machine. The positioning and alignment of the mask are critical for pattern resolution in processes requiring multiple lithographic steps. In our case, involving a single lithography with one mask, precise alignment is less critical. However, vacuum contact between the mask and the wafer remains important for lithographic resolution and for ensuring the dimensional accuracy of the resistance channels in our application. The exposure dose ranges from 90 to 140 mJ and lasts only a few seconds.

After exposure, the wafers are baked at 105°C for 120 seconds to initiate the cross-linking reaction of the photoresist.

Finally, the wafers are manually immersed in AZ 726 MIF developer for 45 seconds to dissolve the exposed photoresist. They are then rinsed with deionized water, cleaned with methanol, and dried using an N2 nitrogen gun.

All photolithography steps are carried out in a specific chamber within the cleanroom, where the lighting is yellow to eliminate ultraviolet light and prevent unintended exposure of the photoresists before development.

To ensure the photolithography process was successful and yielded good resolution, the wafers were analyzed under a microscope. For resolution verification, particular attention was paid to the alignment marks visible in Figures 4.10 and 4.11. These alignment marks, of various sizes, help assess the equipment's capability to reproduce patterns of specific sizes and complexities, as well as to determine the resolution limit. The presence of these marks provides confidence in the quality of our lithography. However, it does not guarantee the absence of isolated defects in the photolithography process.

Photolithography			
Parameters	**Wafer priming**	**Spin coating**	**Pre-exposure baking**
Equipment	LPIII oven	SUSS Gamma	SUSS Gamma
Input	HDMS	3 ml of Photoresist AZnLof5510	/
Temperature [K]	373.15	298.15	363.15
Duration [s]	1380	60	60
speed [rpm]	/	3000	/

Photolithography			
Parameters	**Exposure**	**Post-exposure baking**	**Development**
Equipment	SUSS MA6	SUSS Gamma	Wet bench
Input	/	/	15 ml of Developer AZ 726 MIF
Temperature [K]	298.15	378.15	298.15
	a few seconds	120	45
Exposure dose [mJ]	90-140	/	/
Type of contact	vacuum	/	/

Table 4.6: Parameters of photolithography

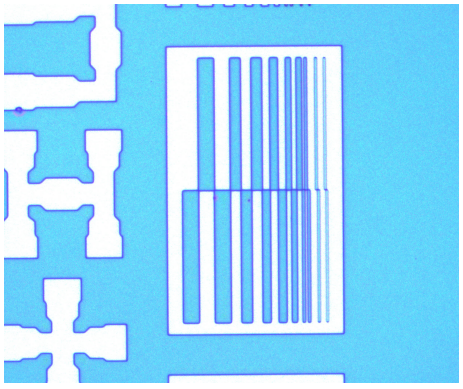

Figure 4.10: Microscope image of resin patterns after lithography. Wafer with gold contacts

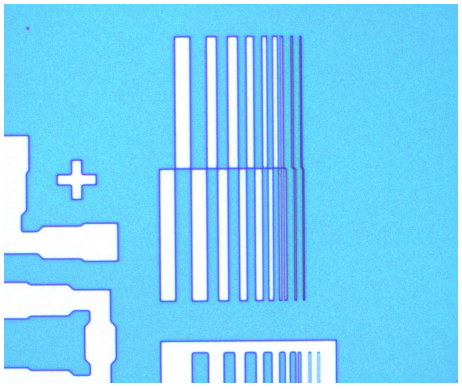

Figure 4.11: Microscope image of resin patterns after lithography. Wafer with gold contacts

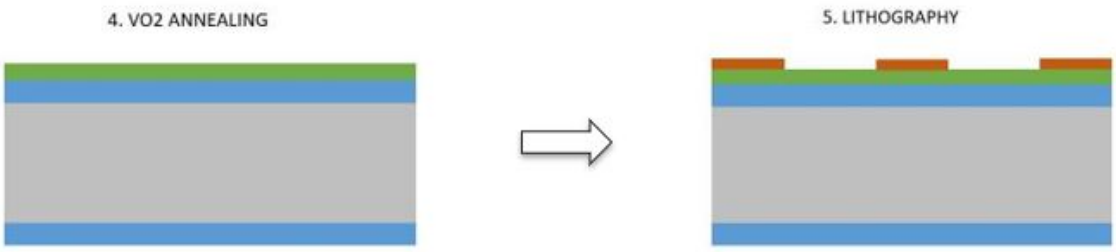

Figure 4.12: Cross section of the photolithography microfabrication step [37]. The color gray represents Si, while blue represents SiO2, green is crystallized VO2 and orange the photoresist.

4.6 Metallization

With the pattern for the metallic contacts delineated on the wafer by the remaining photoresist, the next step is to deposit the metal across the entire wafer. The remaining photoresist will be removed afterward.

There are various methods to deposit a metal layer on a wafer, such as evaporation and e-beam evaporation, sputtering, chemical vapor deposition (CVD) and plasma-enhanced chemical vapor deposition (PECVD), and electrolytic deposition, among others. However, in our cleanroom, only e-beam evaporation can be used for depositing gold. Consequently, this method was employed to deposit the different metals, ensuring uniformity.

4.6.1 Principle

Metalization by Electron Beam Physical Vapor Deposition (EBPVD) involves directing a beam of electrons at a desired metal, typically placed in a crucible. The metal heats up to the point of evaporation and then condenses on the wafer positioned above. The electrons are accelerated by a magnetic field to increase their kinetic energy, which is transferred to the metal through interactions, converting to thermal energy and heating the metal to its evaporation temperature.

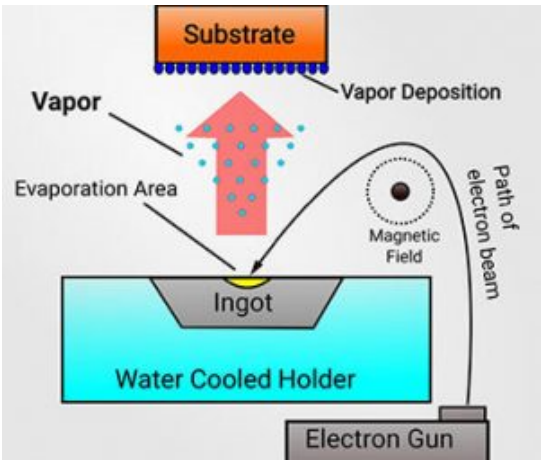

Figure 4.13: principle of Electron Beam Physical Vapor Deposition [22]

It is crucial to note that the deposition chamber is maintained under vacuum to increase the mean free path of both the electrons and the evaporated metal atoms. A longer mean free path for the electrons ensures that they encounter no obstacles before reaching the metal, maximizing energy transfer. Similarly, a longer mean free path for the evaporated metal atoms allows them to condense on the wafer without colliding with other particles, essential for precise control over the quantity and nature of the deposited vapor.

The thickness of the metal layer condensed on the wafer is monitored by a quartz crystal. Once the desired thickness is achieved, the electron beam is halted, the metal cools, and evaporation ceases. The wafer can then be removed from the deposition chamber. Typically, the wafer rotates on its axis during evaporation to ensure uniform deposition. The primary parameters influencing the deposition rate include the type of metal being evaporated, the power of the electron beam, and the quality of the vacuum.

4.6.2 Process

In our process, two different metals were deposited: gold as a reference and Aluminium. Gold was deposited using the Vacotec equipment. To ensure adhesion of gold to the vanadium dioxide, 5 nm of chromium was first deposited, followed by 150 nm of gold. The wafer, along with the gold and chromium crucibles, were loaded the day before the

deposition to achieve a vacuum overnight, reaching a sufficiently low pressure just before deposition. Once the pressure was adequately reduced, the electron gun was activated to first heat the chromium and then the gold. When a stable evaporation rate was attained, the shutter protecting the wafer was opened, allowing the metal to condense on the wafer.

It is important to note that the Vacotec equipment does not rotate the wafer on its axis, potentially resulting in a slight thickness gradient across the wafer, as the crucible containing the metal is not directly aligned with the wafer. Upon reaching the desired metal layer thickness, the electron beam is stopped, and cold water is circulated around the chamber and crucible for about fifteen minutes to cool them down. Before opening the chamber to retrieve the wafers, warm water is circulated to slightly raise the chamber temperature, preventing condensation on the wafer when the chamber is opened.

Since the Vacotec equipment is reserved for extended periods, Aluminium was deposited using another system, the VST, which also supports EBPVD. The deposition chamber was loaded with the wafer and Aluminium in the morning, and deposition commenced in the afternoon after reaching a sufficiently low pressure. Although this equipment allows wafer rotation during deposition to ensure uniform layer thickness, the wafers were not rotated to maintain consistent deposition conditions with those used for gold in the Vacotec system.

Metallization		
Parameters	**Gold deposition**	**Aluminium deposition**
Equipment	Vacotec	VST
Pressure [HPa]	1.42 E-6	1.1 E-5
Deposition rate [Å/sec]	2	2.23
Deposition Duration [s]	772	693
Thickness [nm]	150	150

Table 4.7: Parameters of metallization

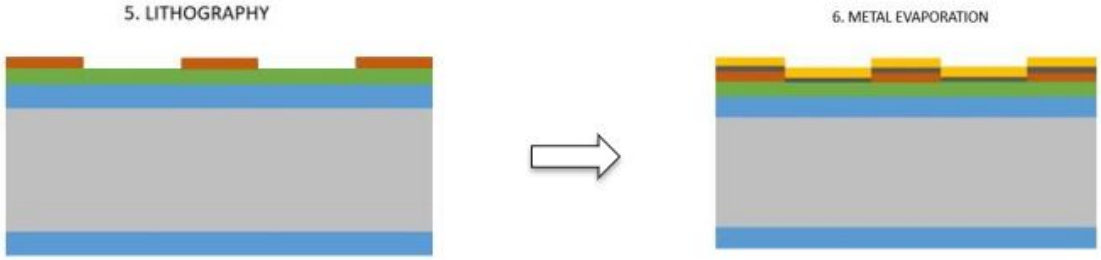

Figure 4.14: Cross section of the metallization microfabrication step [37]. The color gray represents Si, while blue represents SiO2, green is crystallized VO2, orange is the photoresist and yellow the metal.

4.7 Lift-off

Ultimately, to complete the process, the remaining photoresist and the metal deposited on top of it must be removed.

4.7.1 Principle

The principle of lift-off is relatively straightforward. The wafer is immersed in a solvent bath that dissolves the remaining photoresist. As the photoresist dissolves, the metal on top of it loses its attachment to the wafer and floats in the solvent. To facilitate the lift-off process, the solvent can be heated, and vibrations may be induced. The parameters influencing lift-off include the choice of solvent, bath temperature, duration, and the nature of induced agitation.

This final fabrication step is delicate, as several issues may arise. For instance, the floating metal in the solvent may redeposit onto another area of the wafer, the photoresist might not dissolve properly, preventing the metal from detaching, or the metal may coat the sidewalls of the photoresist, creating a junction between the metal that should remain on the wafer and the metal that should be removed.

Despite these potential challenges, lithography and lift-off are widely used for inter-metallic connections due to their ability to produce precise and well-defined metallic patterns, compatibility with metals that are difficult to etch (such as gold), and the simplicity of the process.

4.7.2 Process

For this process, wafers with the same metal were successively immersed in two baths of 700 ml of DMSO (dimethyl sulfoxide) solvent. Wafers with different metals were not immersed in the same solvent bath to prevent cross-contamination. Additionally, two solvent baths were used: the first to remove most of the photoresist and the overlying metal, and the second to prevent redeposition. The baths are heated to 60°C and agitated by ultrasonic vibrations. Each immersion in the solvent bath lasts for 5 minutes. After this period, the wafers are rinsed with methanol and deionized (DI) water, and finally, they are dried using an N2 gun.

Parameters	**Lift-off**
Equipment	Wet bench
Composition	DMSO (C_2H_6OS)
vibrations induce in the baths	ultrasonic
Temperature of the baths [K]	333
Total duration of the baths [sec]	600

Table 4.8: Parameters of lift-off

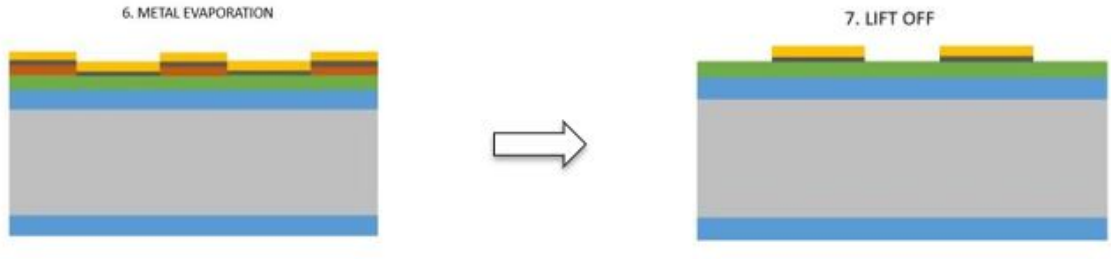

Figure 4.15: Cross section of the metallization microfabrication step [37]. The color gray represents Si, while blue represents SiO2, green is crystallized VO2 and yellow the metal.

All these procedures are carried out under a dedicated wet bench for lift-off in the cleanroom. Finally, our devices are ready to be used for characterization.

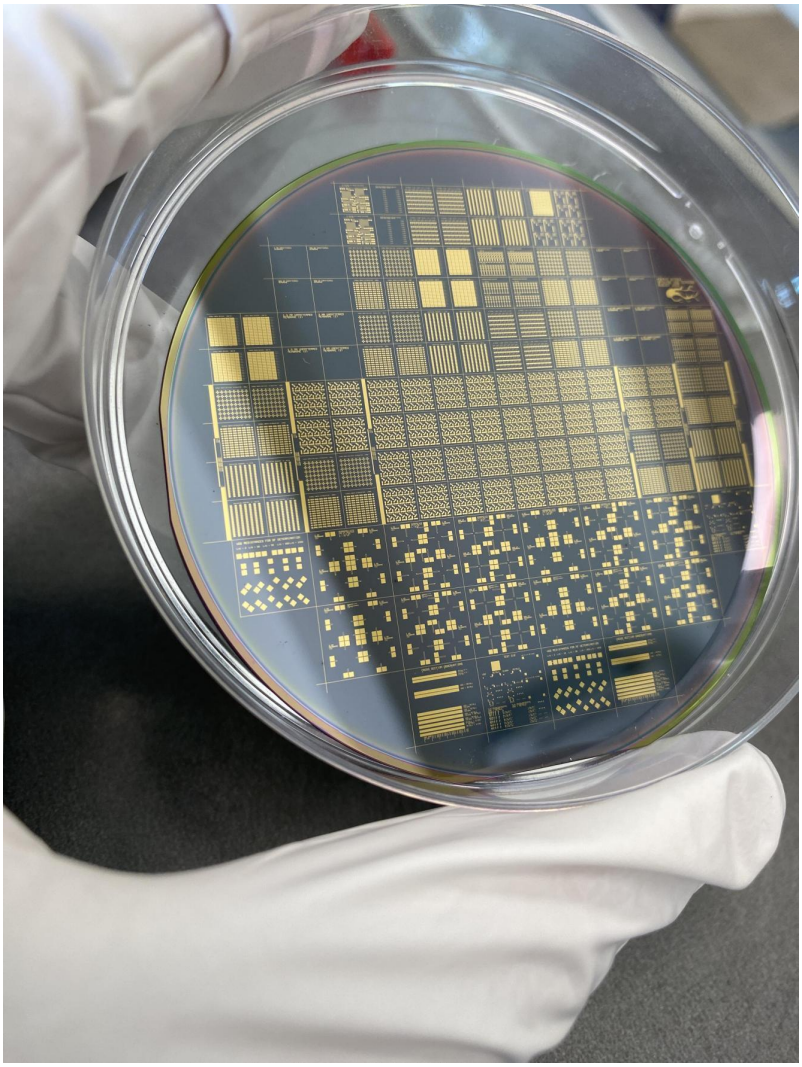

Figure 4.16: Photo of the gold wafer after all the fabrication steps

Chapter 5

Caracterisation

Following fabrication, the devices are now ready for use and analysis. This chapter will examine and compare the differences between resistors with gold contacts and those with aluminium contacts. Initially, the samples will be observed under a microscope and analyzed with a Raman spectrometer, with a particular focus on the vanadium dioxide layers, to perform characterization. Subsequently, electrical measurements will be conducted using the PM8PS prober to confirm the proper transition of VO2 and to characterize the sheet resistance of the VO2 layers through four-point probe resistivity measurements. Additionally, contact resistances of gold and aluminium will be deduced using Transfer Length Method (TLM) structures.

Given the potential applications of vanadium dioxide presented in section 2.1.3, it is imperative that the devices undergo numerous transition cycles. Considering that the recycling of microelectronic devices poses significant challenges due to the minute quantities of metal present on the wafers [16], it is of interest to investigate the ageing of these structures to optimize their operational lifespan. Therefore, in the final section of this chapter, ageing tests will be performed to analyze the notable differences between the two metals and to assess whether aluminium could be considered a viable alternative to gold for the contacts of these resistors.

In the remainder of this chapter, it should be noted that all tests were conducted on only two wafers: one with gold metal contacts and the other with aluminium contacts.

5.1 Observations

5.1.1 SEM

Before initiating the characterization and differentiation of resistances with aluminium and gold contacts, the channel lengths of various randomly selected resistors on the wafers were verified to ensure the photolithography and lift-off processes were successful. This was measured using a Scanning Electron Microscope (**SEM**). The SEM operates by utilizing a focused electron beam that scans the surface of the sample. The electrons interact with the sample surface, generating various signals that are then translated into detailed images of the sample's topography and composition. This method provides high-resolution images of the sample surface. The SEM operates under vacuum conditions for several reasons: firstly, to prevent collisions between the electron beam and ambient air atoms; secondly, to enhance signal detection; and finally, to protect the equipment, including the electron beam emitter and detectors [34][35].

Figure 5.1: EISS focused ion beam scanning electron microscope (SEM) used in the Winfab lab

To ensure comparability between SEM images, it is crucial to maintain a consistent electron beam power. In this study, a beam power of 3kV was maintained for each image captured by the microscope. Other parameters, such as brightness, contrast, and zoom level, were adjusted as necessary to achieve optimal image quality. However, it is observed across the various SEM images that the gold contacts appear brighter than the aluminium contacts. This phenomenon is attributed to the higher electron backscattering of gold compared to aluminium, due to its greater electron density and atomic number [28].

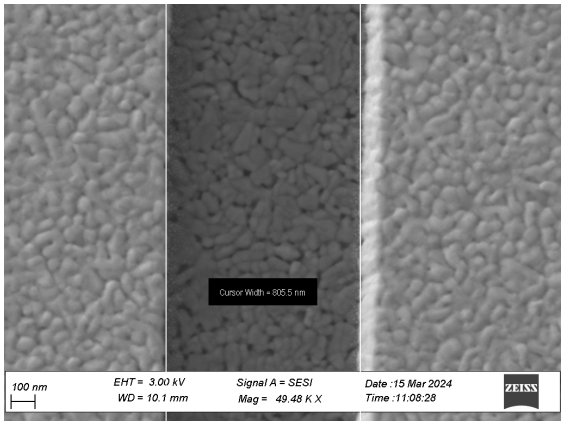

Figure 5.2: SEM imageing of device's channel with gold contacts. Desired length during fabrication = 800nm

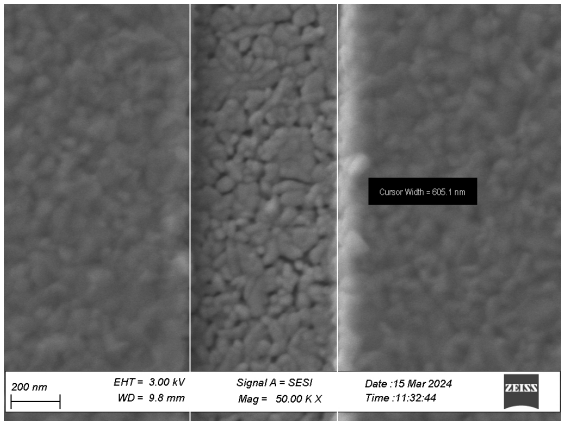

Figure 5.3: SEM imageing of device's channel with aluminium contacts. Desired length during fabrication = 600nm

Figures 5.2 and 5.3 reveal that the resistor channels are very close to the desired dimensions. As previously mentioned, the inspection of alignment marks after photolithography provides reassurance that both the photolithography and lift-off processes were successful, and that the resolution achieved is sufficient. However, this does not eliminate the possibility of localized defects on the wafer, which may render certain devices unusable.

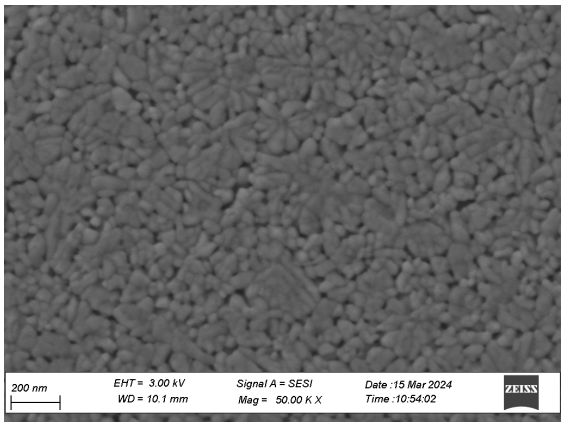

Figure 5.4: SEM image of the surface of the vanadium dioxide layer. Wafer with gold contacts

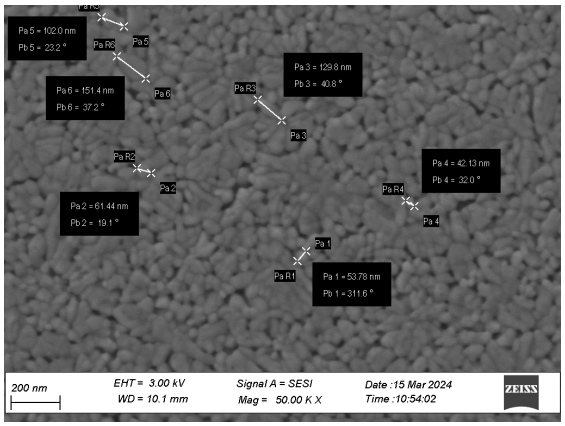

Figure 5.5: SEM image of the surface of the vanadium dioxide layer. Wafer with gold contacts

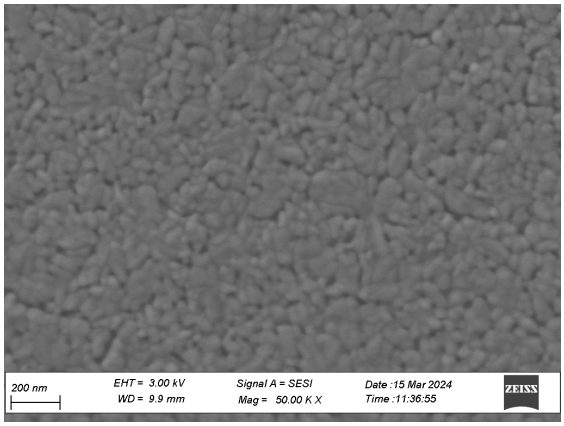

Figure 5.6: SEM image of the surface of the vanadium dioxide layer. Wafer with aluminium contacts

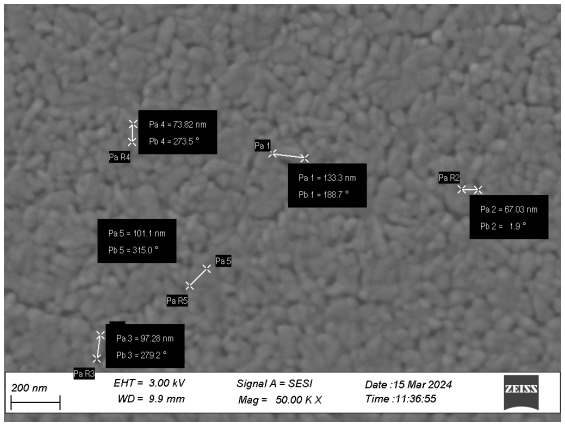

Figure 5.7: SEM image of the surface of the vanadium dioxide layer. Wafer with aluminium contacts

Utilizing the SEM, we examine the surface of the vanadium dioxide layer. Comparing images 5.4 and 5.6, a similar surface of vanadium dioxide is observed. There appears to be slightly less space between grains on the image, indicating a marginally higher density on the wafer with aluminium contacts. However, this difference is subtle. Surface grain sizes are comparable on both wafers, though caution is needed in comparison as depth variations could differ significantly. As intended, the grain sizes are relatively small and remain below the minimum channel length of our devices (600 nm). As explained in the state of the art (see 2.1.4), large grains shows more cycle-to-cycle variation. In contrast, smaller grains typically exhibit lower resistance in their insulating phase and shows less

variability[3], crucial for measurement consistency.

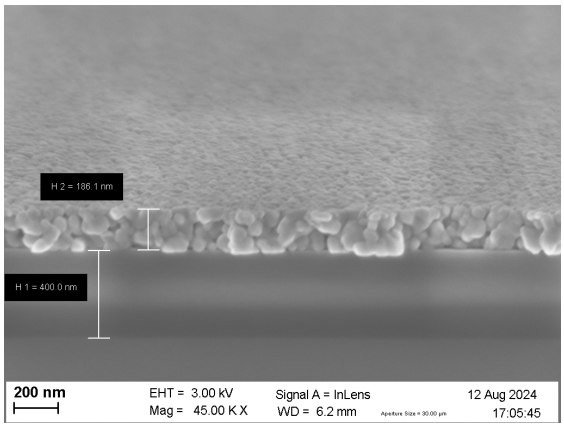

Figure 5.8: SEM image of the section of the wafer with gold contacts

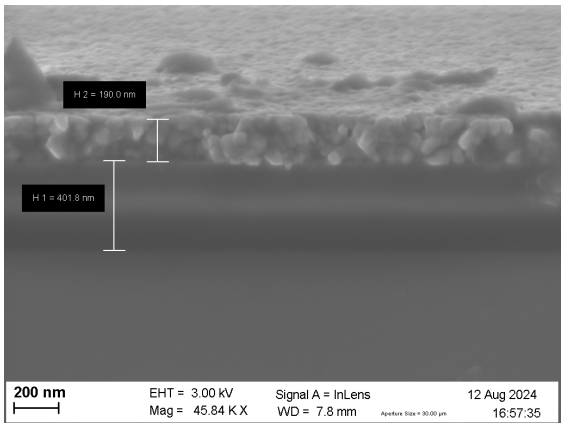

Figure 5.9: SEM image of the section of the wafer with aluminium contacts

Figures 5.8 and 5.9 present the cross-sectional views of the wafers, enabling verification of the deposited layer thicknesses. It is observed that the layer thicknesses conform to the specified requirements. However, this thickness was only verified at a single location near the center of the wafer.

5.1.2 Raman

Following SEM analysis, samples are analyzed using a Raman spectrometer to verify the stoichiometry of our vanadium dioxide layer. Raman spectroscopy is a technique for characterizing material composition and structure by illuminating the sample with monochromatic light and measuring the frequency shift of scattered light. These shifts produce a unique frequency spectrum for each molecule, enabling identification of molecules present on the wafers [13] [40].

To interpret these spectra, one needs to examine the positions of the peaks and compare them with litterature (Table 5.1). Differents known peaks of differents Vanadium oxides found in the literature are presented in the annexes (see A.1). Additionally, assessing crystallinity involves measuring the peak widths at half-maximum intensity. A narrower peak indicates higher crystallinity with a more ordered network, whereas a broader peak suggests greater disorder in the material's network structure.

Although the spectrum peaks of vanadium dioxide on the wafer with gold contacts (red curve) are lower than those on the wafer with aluminium contacts (blue curve), the peaks of both curves can be attributed to VO2 as seen in Table 5.1. To compare the spectra, the peak widths at half-maximum intensity should be measured, and the difference in our case is imperceptible. Additionally, the graph 5.10 shows a peak at 520 [1/cm], attributed to the silicon wafer, which is used to calibrate the Raman spectrometer.

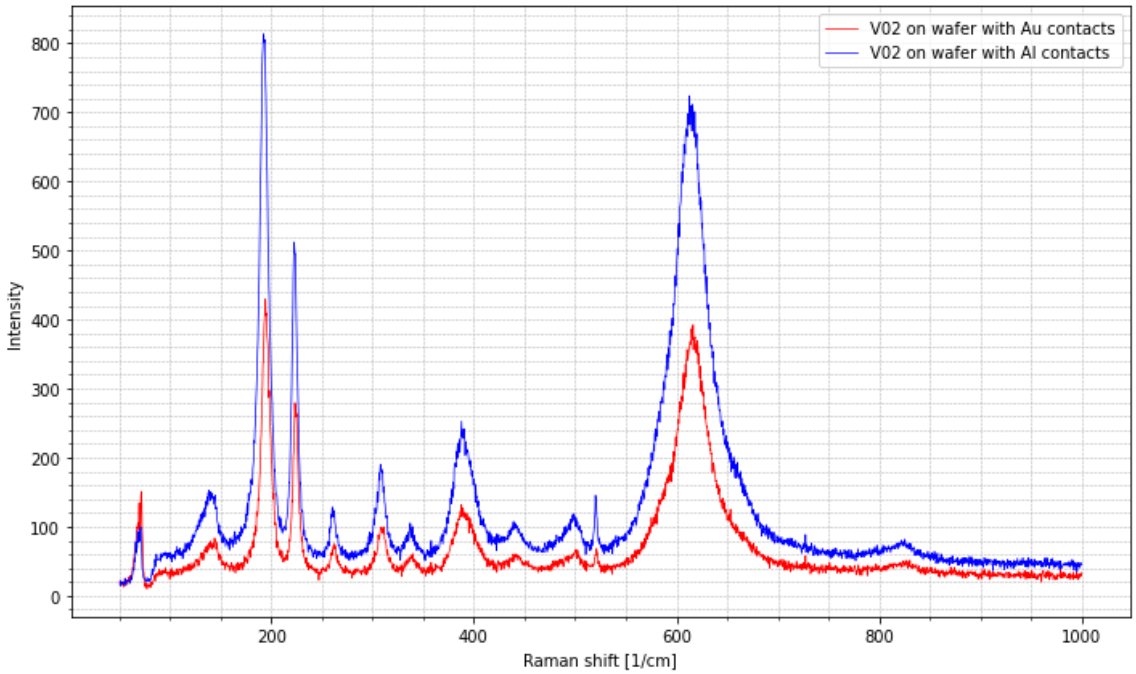

Figure 5.10: Raman spectrum of our VO2 layers on our 2 wafers

VO_2 (M1)	
Peak (cm^{-1})	**Description**
143	
193	
224	
261	
310	
339	
391	
443	
449	
482	small shoulder
590	small shoulder
614	
665	small shoulder
824	very weak

Table 5.1: Raman peaks for VO_2 (M1) phase A.1

5.2 Proper Functioning

Following the initial SEM observations, the first electrical characterizations are conducted. The primary verification is to ensure that VO2 transitions properly from an insulating to a metallic state. This is achieved by gradually increasing the voltage applied to the resistor contacts. As the voltage increases, the current also rises progressively, and Joule heating raises the temperature until it reaches the transition temperature, converting VO2 from an insulating to a metallic state. These measurements are performed using the PM8PS.

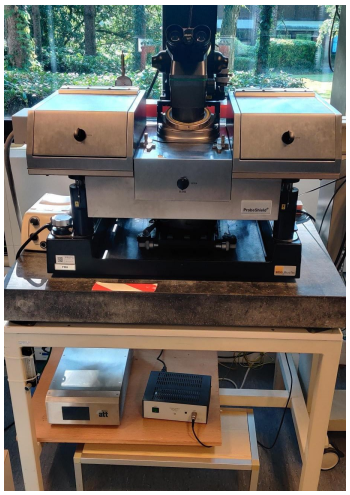

Figure 5.11: Photo of the PM8PS equipment in Welcome lab

The PM8PS is a prober station that allows for precise injection and measurement of currents or voltages on microscopic devices. Once the wafer is placed on the chuck within the measurement chamber, a vacuum is created between the wafer and the chuck to secure the wafer during measurements. The chuck is capable of heating. For each measurement, the temperature was set at 35°C to ensure that the VO2 remained in the insulating regime but above ambient temperature, preventing room temperature variations from affecting the measurements. Probes were carefully positioned using micrometers on the desired metal contacts of the wafer.The tips of the four probes are replaceable. The fact that the tips are made of a different material than the contact of the devices can also significantly increase the measured series resistance. For our measurements, eight tips dedicated exclusively to our measurements were used four for gold contacts and four for aluminium contacts to avoid contamination of contacts and probes. All measurements were conducted with the light turned off to prevent heat from affecting the results. Additionally, nitrogen was introduced into the measurement chamber, even though it is not airtight, to minimize oxidation from ambient air. The heat (from the chuck and the currents passing through the devices) significantly accelerates oxidation [7].

Thus, the initial current-voltage curves are obtained in both V-driven and I-driven modes. V-driven indicates that the parameter being varied is the voltage, whereas I-driven varies the current, resulting in different characteristic curves already presented in the state of the art (see Fig 2.2). Each electrical measurement with the PM8PS involves performing what is known as a cycle. Since vanadium dioxide exhibits hysteresis, meaning the temperature and consequently the voltage or current required for VO2 to transition from an insulating to a metallic state is not the same as that required to transition back from metallic to insulating, it is useful to conduct complete cycles to gather comprehensive information. Hence, when referring to a cycle in the remainder of this report, it denotes the process of gradually increasing the current or voltage to the desired value and then decreasing it back to zero to observe both transitions.

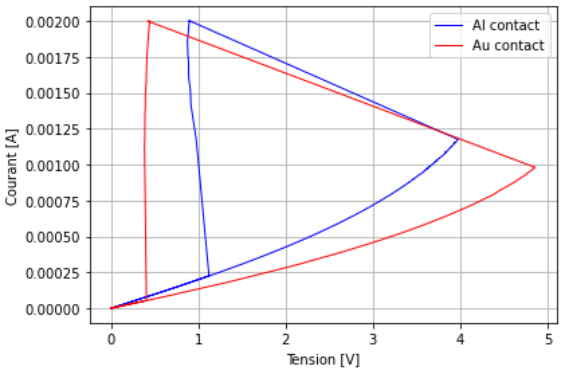

Figure 5.12: V-driven cycle for device of L=1.2um and W=10um at 308.15K

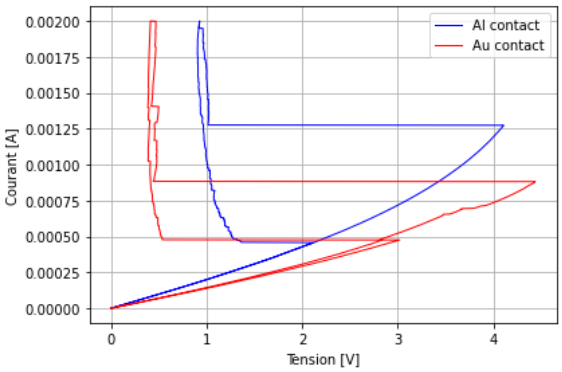

Figure 5.13: I-driven cycle for device of L=1.2um and W=10um at 308.15K

The aim of these initial tests was to verify that vanadium dioxide transitions properly and to observe the characteristic curves (as in the state of the art Fig 2.2). This objective has been successfully met. However, the exact characteristic V-driven curves with hysteresis cycles, commonly observed in most literature on the subject, are not fully replicated in our results. This deviation is attributed to the imposition of a maximum current threshold of 2mA. According to Ohm's law, when VO2 transitions from an insulating to a metallic state, its resistance decreases by several orders of magnitude. Consequently, since the voltage is controlled, the current increases abruptly, which could potentially cause irreversible damage. Therefore, the injected current is limited to prevent such damage. Nevertheless, the abrupt change in resistivity is clearly observed in Figures 5.12 and 5.13, indicating that vanadium dioxide undergoes a state change.

To isolate the resistance of VO2 in its two states, four-point probe resistivity measurements are performed [20] [30]. By injecting a current through the outer probes, as shown in Figure 5.14, and measuring the voltage across the inner probes, the resistance of VO2 can be determined using the formula:

$$R_s = \frac{\pi}{\ln(2)} \cdot \frac{V}{I} \tag{5.1}$$

Here, R_s represents the sheet resistance, which is the electrical resistance of a thin layer and equals the material's volumetric resistivity divided by its thickness. This formula is valid only if the distance between the probes s is significantly greater than the thickness t of the vanadium dioxide layer. In our case, the distance s is 100 um, while the thickness of VO2 is less than 1 um, which confirms the validity of this assumption.

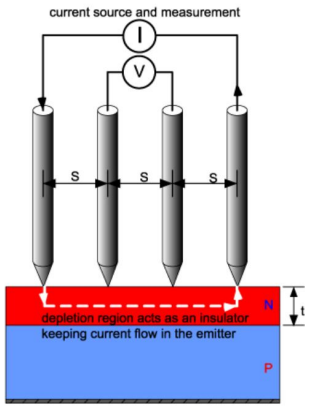

Figure 5.14: Four Point Probe Resistivity Measurements [20]

Applying this method to both gold and aluminium contacts for VO2 in its insulating and metallic states, Figures 5.15 and 5.16 are obtained. By extracting the slopes of the lines, the I/V ratio is determined. The formula 5.1 is then used to find the sheet resistivity R_s. A summary table 5.2 of the slopes of each line and the associated resistivities is provided.

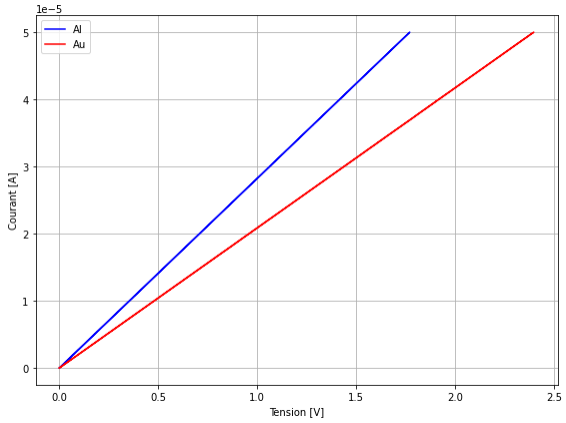

Figure 5.15: 4 point probe resistivity measurement for aluminium and gold contacts at 308.15K

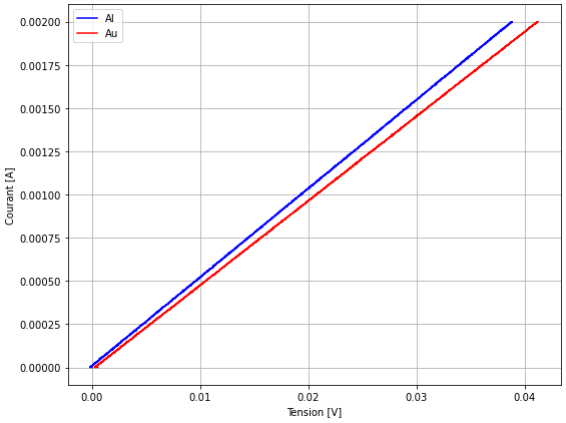

Figure 5.16: 4 point probe resistivity measurement for aluminium and gold contacts at 373.15K

	$V/I[\Omega]$	$R_s[\Omega/\square]$
Al contacts at 308.15K	35 405.62	160 458.27
Au contacts at 308.15K	47 931.87	217 227.23
Al contacts at 373.15K	19.48	88.28
Au contact at 373.15K	20.45	92.68

Table 5.2: Sheet resistivity R_s for aluminium and gold contacts at 308.25K and 373.15K

A difference in sheet resistance of vanadium dioxide between the two wafers is observed in both the insulating and metallic regimes. Several factors may contribute to this discrepancy. Firstly, variations in the thickness of the vanadium dioxide layer between the two wafers could be a factor. Although the sputtering time is the same for both wafers, controlling the exact thickness of the layer is challenging. Variations between different depositions using the AJA (sputtering equipment) can arise due to numerous factors, including slight differences in the deposition atmosphere, the precise distance between the target and the sample, the surface condition of the wafer, and the wear and stoichiometry of the target. Additionally, the grain size also influences the measurements. Although the surface grain sizes appeared comparable between the two wafers in the SEM observations section above, they are not identical. Finally, localized contamination or a specific defect in the vanadium dioxide layer cannot be completely ruled out as explanations for the difference in sheet resistance.

Using the sheet resistance values in both states of VO2 and for the two different metal contacts presented in Table 5.2, the ON/OFF sheet resistance ratio can be calculated, defined as the ratio of the resistances of VO2 in its two phases. An ON/OFF ratio of 1817.6 and 2343.8 is obtained for VO2 with aluminium and gold contacts, respectively.

Now that the resistivity of VO2 on the wafers with gold and aluminium contacts is known, the contact resistances of these materials can be investigated. To achieve this, a transfer length method (TLM) measurement is performed [17][21]. This method involves measuring the resistance between several pairs of metallic contacts deposited on the surface

of the material being tested, with varying distances between the contacts.

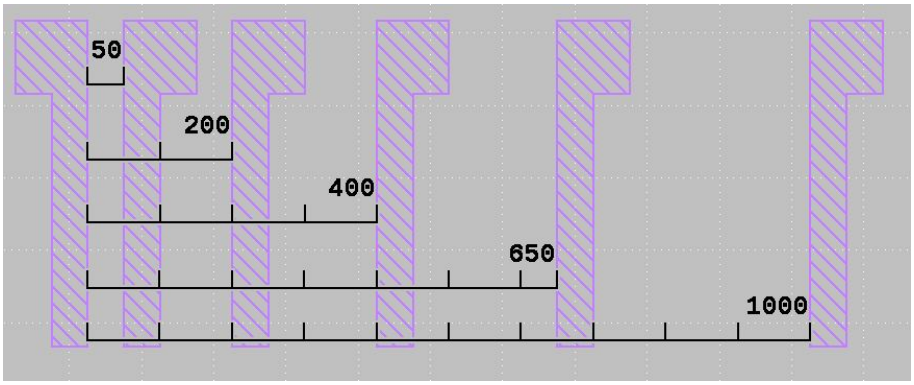

Figure 5.17: TLM contacts

Figure 5.17 illustrates the TLM structures on the wafers. The purple structures in the photo 5.17 represent the metallic contacts, while the gray background represents the VO2 layer. The spacing between the various contacts is 50, 200, 400, 650, and 1000 um. The width W is 450 um.

This setup allows for the isolation of contact resistance and material resistance. The total resistance is given by:

$$R_{Tot} = 2R_m + 2R_c + R_{semi} \tag{5.2}$$

where R_{Tot} is the total resistance, R_m is the metal resistance, R_c is the contact resistance between the metal and the material under study (in this case, VO2), and R_{semi} is the resistance of VO2. The metallic resistance can be estimated based on the resistivity values of the metals provided in Section 3 and the dimensions of the contacts. Assuming a resistivity of 24 n$\Omega * m$ for gold and 28 n$\Omega * m$ for aluminium, with contact dimensions of 150 um on each side and a thickness of 150 nm, the calculated resistance values are 1.6 mΩ and 1.87 mΩ for gold and aluminium, respectively. Given the negligible magnitude of the metal resistance, it can be disregarded. Furthermore, the resistance of vanadium dioxide can be decomposed as $R_{semi} = R_s \frac{L}{w}$. Thus, the total resistance becomes:

$$R_{Tot} = 2R_c + R_s \frac{L}{W} \tag{5.3}$$

where R_c is the contact resistance, R_s is the sheet resistance of vanadium dioxide, and W and L are the width and length of the resistors, respectively.

It becomes evident that by measuring the total resistance while varying the length, one can isolate both the contact resistance and the sheet resistance. Specifically, plotting the total resistance as a function of the resistor length, the y-intercept of the linear regression provides $2R_c$, and the slope of the line yields $\frac{R_s}{W}$

To extract the total resistance for a pair of contacts, the current is incrementally and minimally increased to avoid approaching the metallic regime, and a linear regression of the slope V/I is performed to determine the resistance (see Figures A.2 and A.3 for mor details). The currents range from 0.1 mA for the closest contacts to 2 mA for the most distant ones. This process is repeated for each contact pair of varying lengths to obtain

the total resistance for each distance and for both regimes at 35°C and 100°C, as shown in figures 5.18 and 5.19.

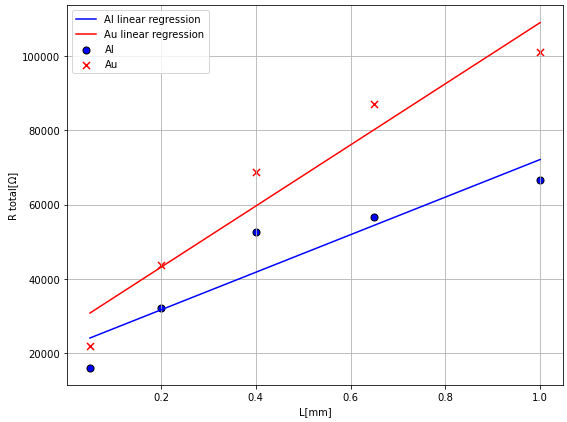

Figure 5.18: TLM measurements for Aluminium and gold contacts at 308.15K

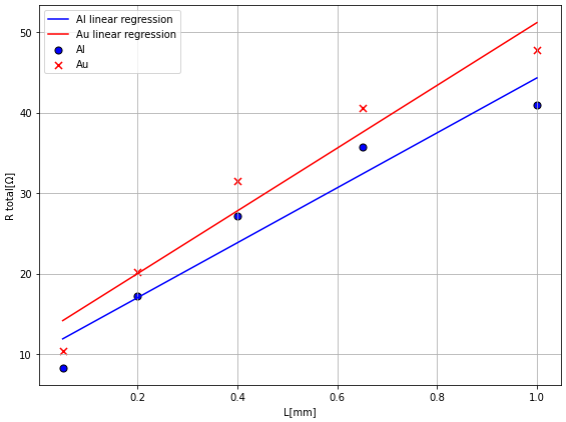

Figure 5.19: TLM measurements for Aluminium and gold contacts at 373.15K

It is observed that the data points do not precisely form a straight line, and as the distance increases, the total resistance decreases relative to the linear regression. This deviation is potentially due to the fact that the VO2 has not been etched, resulting in leakage currents and edge effects. Using these graphs 5.18 and 5.19, the contact resistance can be extracted from the y-intercepts, and the sheet resistance can be determined from the slopes of the lines. These values are summarized in Table 5.3 below.

The observed sheet resistance values of VO2 are significantly lower than those previously calculated in Table 5.2. Determining the exact cause of this discrepancy is challenging, but it may potentially be attributed to edge effects, which could be significant in the case of the TLM structure. In contrast, the formula used for the four-point method assumes precise resistivity, which could explain the lower resistance extracted in this instance.

	R_c [Ω]	R_s/W [Ω/mm]	R_s [Ω/□]
Al contacts at 308.15K	10 738.98	50 665.53	22 799.49
Au contacts at 308.15K	13 310.73	82 448.15	37 101.67
Al contacts at 373.15K	5.09	34.14	15.36
Au contact at 373.15K	6.1	38.99	17.54

Table 5.3: Contact R_c and sheet resistance R_s for aluminium and gold contacts at 308.25K and 373.15K

5.3 Ageing DC

Considering the potential future applications 2.1.3, it is evident that VO2 resistors will need to switch between insulating and metallic states numerous times within short intervals. The aim of this section is to analyze the ageing of the resistors and its effect on gold and aluminium contacts to determine whether aluminium could be a viable alternative to gold.

To investigate this, the decision was made to cycle our two-terminal devices multiple times. By cycling several devices with varying channel lengths, as shown in the photo 4.1, the resistance can be plotted as a function of its length, and TLM measurements can be repeated with our own devices. This approach will allow comparison of contact resistance and VO2 resistance in the insulating state before and after numerous cycles.

The specific procedure followed is as follows: Initially, two controlled high-resolution current cycles (2000 steps of 1 uA up to 2 mA and 2000 steps to return to 0) are performed on five new devices with different channel lengths, for both gold and aluminium. The channel lengths of the devices used for TLM measurements are L[um] = 1.2, 1.6, 2, 2.4, 3, and the constant width W is 15 um. Two high-resolution measurements are conducted to average the results and reduce noise in the linear regression. High-resolution initial cycles are performed to obtain precise resistance values for comparison after the cycles. These cycles are conducted in I-driven mode to control the injected current, particularly during transitions, and to avoid irreversible damage. As explained earlier, when controlling cycles in voltage mode, the current can reach very high values during transitions due to the sudden drop in VO2 resistance.

Following these two initial cycles, 100 low-resolution cycles in I-driven mode are performed solely to transition the VO2. The choice of 100 cycles was made because it already took one hour per resistor (10 in total) on the PM8PS and would allow for the initial observation of differences between gold and aluminium. These cycles are performed in I-driven mode to protect the VO2 from excessive current during transitions. Finally, two additional high-resolution I-driven cycles are carried out to precisely compare resistance values and assess the impact of the 100 transitions on these values. All measurements were conducted at 308.15 K. This protocol is summarized in Table 5.4.

#	Steps		
	number of cycles	**measurement type**	**resolution**
1	2	current driven(2mA max)	high (4000 points)
2	100	current driven(2mA max)	low (10 points)
3	2	current driven(2mA max)	high (4000 points)

Table 5.4: First protocole to investigate the difference between aluminium and gold contacts ageing at 308.15K. Dimensions of the devices tested : L[um]=1.2,1.6,2,2.4,3 and W[um] = 15

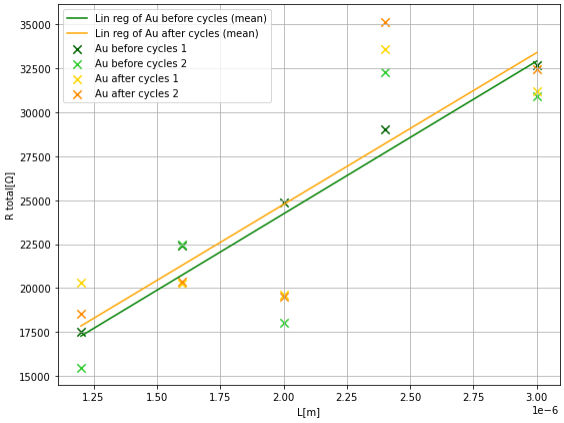

Figure 5.20: TLM measurements for gold contacts before and after 100 cycles at 308.15K

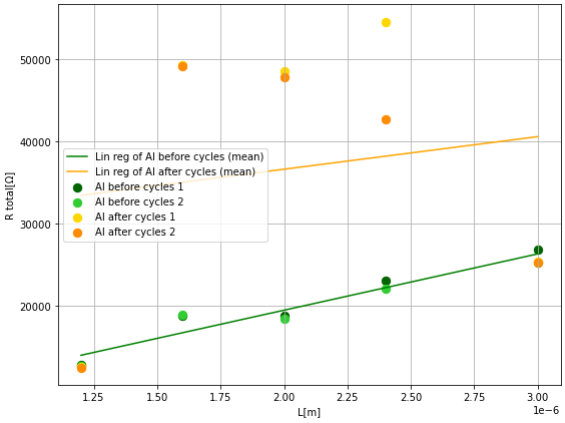

Figure 5.21: TLM measurements for Aluminium contacts before and after 100 cycles at 308.15K

We calculate the total resistance by performing a linear regression in the insulating state. Specifically, we perform a linear regression on the first 100 measured points. In this case, we consider points up to 100 uA, given our 1 uA step size. By doing so, we remain well within the insulating regime and maintain a linear relationship between voltage and current.

By plotting the total resistance as a function of length, we obtain the graphs 5.20 and 5.21. On these graphs, crosses represent gold, and points represent aluminium. The green colors denote measurements from the first two cycles conducted on the devices, while the yellow colors represent measurements from the two cycles performed after the 100 low-resolution cycles. The lines represent the linear regressions of the average measurements taken before (green) and after (yellow) the 100 cycles.

It can be observed from graphs 5.20 and 5.21, that two measurements are never exactly the same. Indeed, measurements face significant fluctuations such as cycle-to-cycle variations and device-to-device variations already presented in section 2.1.4. Moreover, the VO2 layer was not etched, which could also introduce edge effects and other artifacts.

Therefore, it is challenging to extract precise and reliable values for contact resistance and sheet resistance due to the various uncontrollable factors. Linear regressions help visualize trends and the effects of ageing but are not reliable enough to extract exact values for contact and sheet resistances. Thus, we will now refer to total resistance and analyze the impact of the cycles on it.

Based on the linear regression, it appears that for gold, the 100 cycles slightly increase the total resistance, although more tests and measurements are needed to confirm this due to measurement variations. However, there is a noticeable increase in resistance after 100 cycles for aluminium contacts, especially for devices with channel lengths of 1.6, 2, and 2.4 um. Given these intriguing results, we decided to examine these devices with SEM to determine if there were observable impacts of the 100 cycles on the appearance and roughness of our devices. The images obtained are shown below.

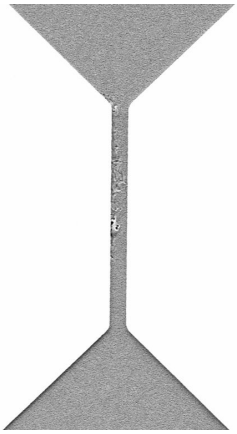

Figure 5.22: SEM image of the device's channel after 100 cycles. Characteristic of the device: L[um]=1.2, W[um]=15, gold contacts

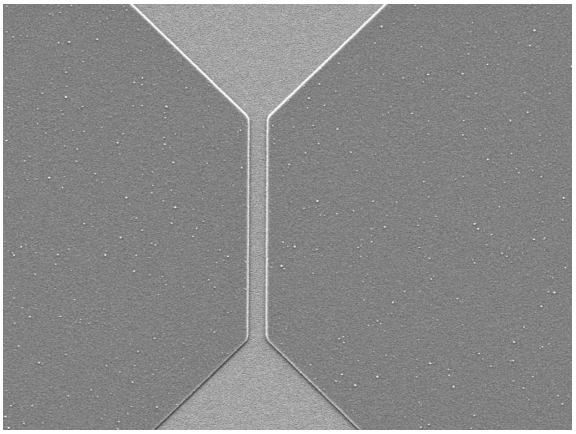

Figure 5.23: SEM image of the device's channel after 100 cycles. Characteristic of the device: L[um]=1.2, W[um]=15, aluminium contacts

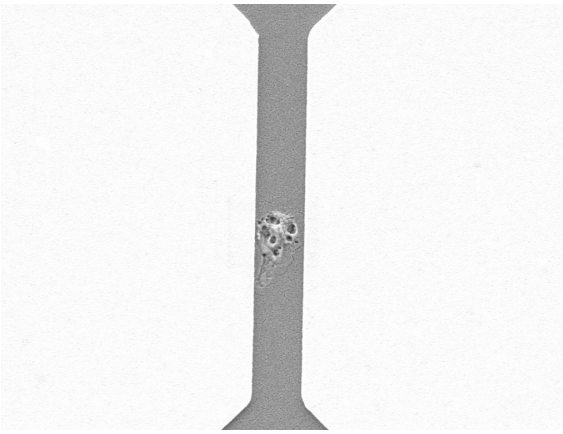

Figure 5.24: SEM image of the device's channel after 100 cycles. Characteristic of the device: L[um]=2, W[um]=15, gold contacts

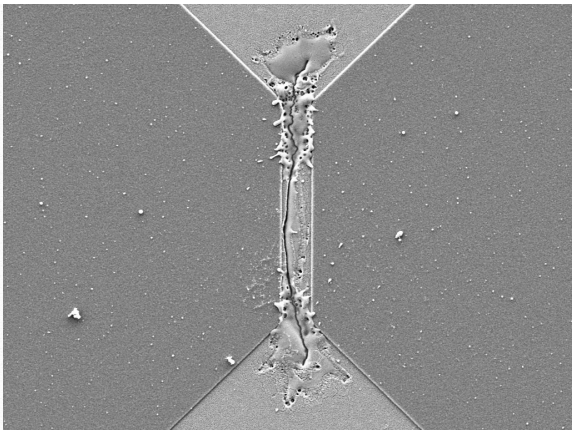

Figure 5.25: SEM image of the device's channel after 100 cycles. Characteristic of the device: L[um]=2, W[um]=15, aluminium contacts

The images 5.22, 5.23, 5.24, and 5.25 illustrate the devices, specifically their channels with lengths of 1.2 um and 2 um, for both gold and aluminium contacts following 100 cycles. As previously stated in Section 3.1.1, these images were captured at 3 kV. The gold contacts appear brighter than the aluminium contacts in the SEM images due to the higher electron backscattering effect associated with gold. Images of channels with other dimensions can be found in the appendices section A.3.

The images reveal degradation in the channels compared to intact devices. For channels with gold and aluminium contacts measuring 1.2 um and 3 um, the degradation appears relatively minor. In contrast, significant degradation is observed in aluminium channels measuring 1.6 um, 2 um, and 2.4 um. This observation aligns with the results indicating a pronounced change in resistance for devices of these dimensions after 100 cycles.

The article [38] outlines several potential forms of damage. Initially, a superficial layer of VO2 is observed to melt, which can slightly decrease the resistance. As the current increases, leading to elevated temperatures near the metallic filament formed during the transition, VO2 undergoes melting and coalescence into microdroplets. This process results in an irreversible degradation of the insulator-to-metal phase transition and its associated hysteresis. Ultimately, at excessively high currents, VO2 ablation occurs in the regions traversed by the current. These deteriorations are likely attributed to the formation of a metallic filament through percolation when the VO2 grains begin to switch, which absorbs the majority of the current. This leads to a sudden drop in resistance, short-circuiting the circuit and causing a spike in current. The Joule heating rapidly intensifies in the switched region, leading to the melting and eventual ablation of VO2 along the filament.

These findings suggest that devices with aluminium contacts may experience more severe or, at the very least, faster degradation compared to those with gold contacts. Given the potential applications, this presents a significant issue if aluminium is to replace gold contacts with regard to durability.

To investigate a potential difference in ageing between aluminium and gold contacts suggested by the previous experimental results, a more detailed protocol has been established. This involves examining the channels of three resistors with varying lengths under SEM. The selected dimensions are L = 0.6 um, 2 um, and 6 um with W = 5 um for both gold and aluminium contacts. Additionally, Raman spectroscopy will be used to analyze the vanadium dioxide within the channels to determine whether oxidation occurs when a current passes through. It is known that heat facilitates oxidation [7], and this approach aims to verify whether differences in resistance before and after experimentation are attributable to changes in stoichiometry caused by oxidation. Raman spectroscopy can only be applied to the larger channels (L = 2 um and 6 um) as the spectrometer's beam is too broad for smaller channels.

Following the initial observations of pristine resistors, a controlled high-resolution current cycle will be performed (4000 steps of 0.5 uA to reach 2 mA and 4000 steps to return to 0). Subsequent analyses will be conducted using SEM and Raman spectroscopy to assess the effects of the first cycle on the resistors. Next, three high-resolution current-controlled cycles will be followed by three high-resolution voltage-controlled cycles (a total of 8000 points as before). Voltage-controlled cycles are chosen for easier comparison as they are more reproducible and do not exhibit the pronounced Negative Differential Re-

sistance (NDR) which shows significant stochasticity that we can find on Fig 2.2. Finally, the resistors will undergo 100 low-resolution current cycles to reduce the cycle time. After this, the resistors will be examined once again using SEM and Raman spectroscopy before undergoing three additional high-resolution voltage and current cycles to compare the resistance differences before and after the 100 cycles. This protocol is summarized in the table below 5.5.

#	**Steps**		
	number of cycles	**measurement type**	**resolution**
1	/	SEM	/
2	/	Raman	/
3	1	current driven (2mA max)	high (8000 points)
4	/	SEM	/
5	/	Raman	/
6	3	current driven (2mA max)	high (8000 points)
7	3	voltage driven	high (8000 points)
8	100	current driven (2mA max)	low (10 points)
9	/	SEM	/
10	/	Raman	/
11	3	current driven (2mA max)	high (8000 points)
12	3	voltage driven	high (8000 points)

Table 5.5: Second protocole to investigate the difference between aluminium and gold contacts ageing at 308.15K. Dimensions of the devices tested : L[um]=0.6,2,6 and W[um] = 5

Figures A.10 through A.14 in the appendices display the voltage cycling experiments.

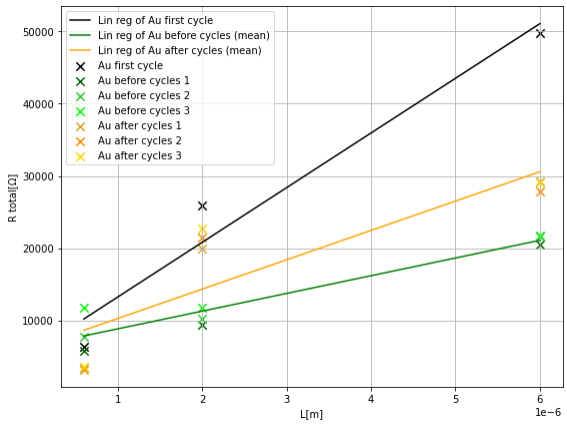

Figure 5.26: TLM measurements for gold contacts before and after 100 cycles at 308.15K

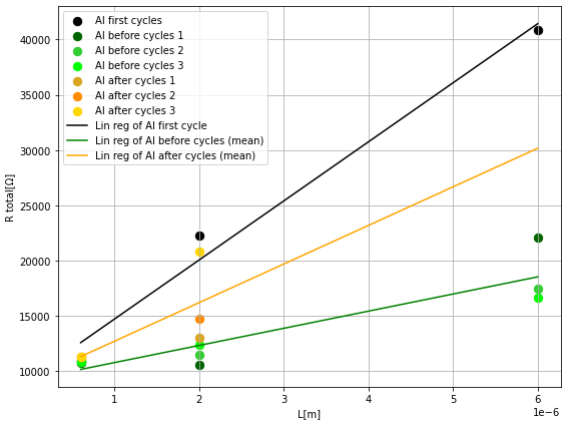

Figure 5.27: TLM measurements for Aluminium contacts before and after 100 cycles at 308.15K

The graphs 5.26 and 5.27 illustrate the total resistance as a function of channel length before and after 100 cycles for both gold and aluminium contacts in the insulating state of VO2. As with the graphs 5.20 and 5.21, the green color represents the resistance measurements taken before the 100 cycles, while the yellow color represents measurements after the 100 cycles. Black points indicate the resistance measurements from the very first cycle experienced by the devices. The lines on the graphs are linear regressions of the average measurements taken before and after the 100 cycles, which aid in identifying trends. No measurements were conducted on the device with aluminium contacts and a channel length of 6 um after the 100 cycles, as it no longer transitioned to a metallic state. Analysis of the linear regressions reveals a common trend for both metals: an initial increase in resistance followed by a decrease in resistivity during subsequent cycles, with a slight increase in resistivity observed after the 100 cycles.

To facilitate comparison, the total resistance as a function of the number of cycles for each channel length is displayed in figures 5.28, 5.36, and 5.44.

The graph 5.28 depicts the total resistivity ($2R_c + R_s \frac{L}{W}$) in the insulating state (at very low current) as a function of the number of cycles. Red crosses represent the resistivity of VO2 with gold contacts, while blue points represent the resistivity with aluminium contacts.

It is observed that the resistivity of VO2 with aluminium contacts remains relatively stable, around $11k\Omega$, as the number of cycles increases. Although some variation is present, it can be attributed to cycle-to-cycle variations. In contrast, significant changes are noted for VO2 with gold contacts. Specifically, the resistivity increases substantially after the first cycle, nearly doubling by the fourth cycle. After 100 cycles, the resistivity decreases sharply to approximately one-third of its value at the fourth cycle, and then rises slightly.

SEM images 5.29, 5.30, and 5.31 for the device with gold contacts show no notable damage or surface modifications to the VO2 layer in the channel before and after the first cycle. However, changes in the appearance of the grains within the channel are evident after 100 cycles, particularly visible in the zoomed-in SEM image 5.32. This observation supports the resistance value trends depicted in graph 5.28, indicating a significant increase

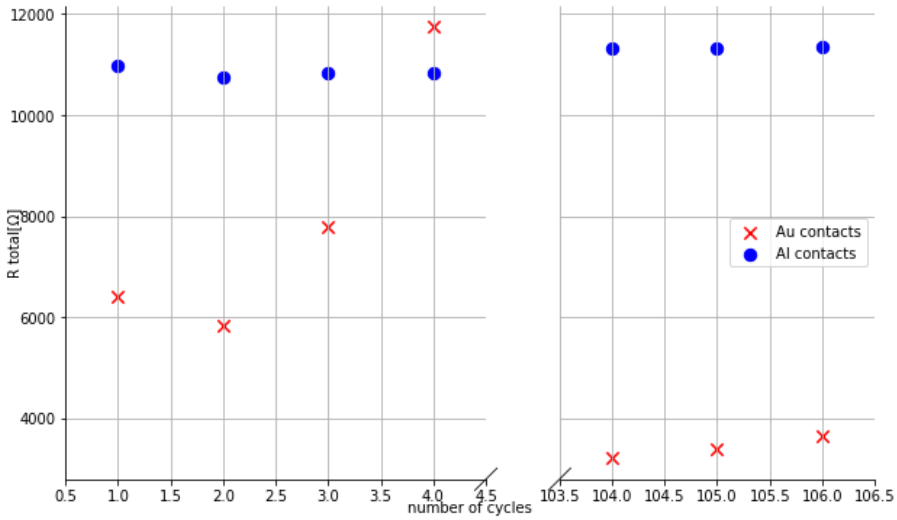

Figure 5.28: Total resistivity measured at 35°C for VO2 with gold and aluminium contacts in function of the number of cycles. Device length L[um]=0.6, Device width W[um]=5.

in resistance by the fourth cycle, which suggests permanent deformation in the channel.

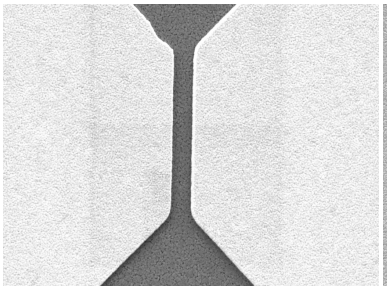

Figure 5.29: SEM image of the pristine device's channel. Characteristic of the device: L[um]=0.6, W[um]=5, gold contacts

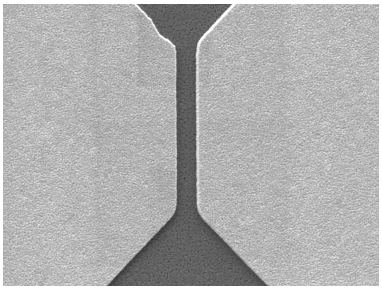

Figure 5.30: SEM image of the device's channel after 1 cycle. Characteristic of the device: L[um]=0.6, W[um]=5, gold contacts

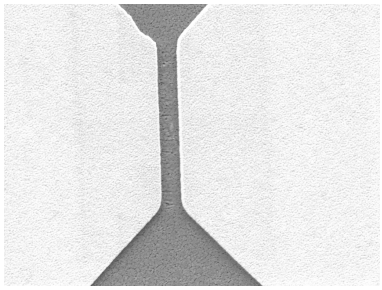

Figure 5.31: SEM image of the device's channel after 100 cycles. Characteristic of the device: L[um]=0.6, W[um]=5, gold contacts

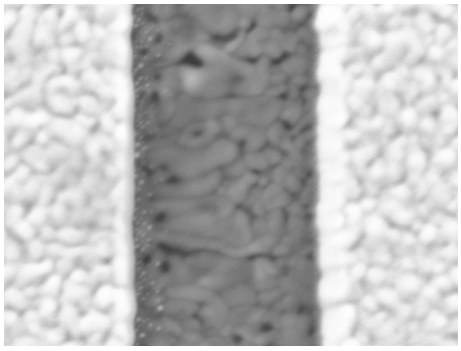

Figure 5.32: Zoom of the device's channel after 100 cycles. 5.31

No notable difference is observed in the vanadium dioxide within the channel of the device with aluminium contacts, even after 100 cycles. This observation corroborates the results presented in graph 5.28, where no significant change in resistance is detected either.

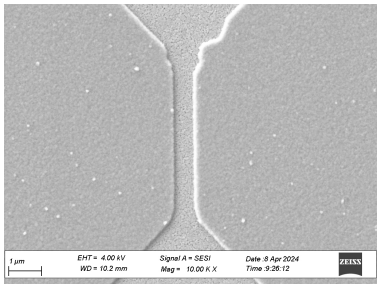

Figure 5.33: SEM image of the pristine device's channel. Characteristic of the device: L[um]=0.6, W[um]=5, aluminium contacts

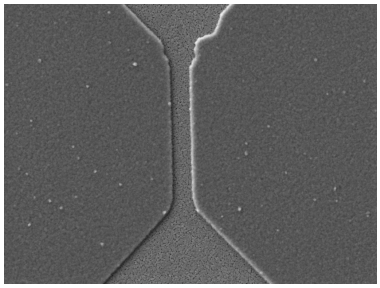

Figure 5.34: SEM image of the device's channel after 1 cycle. Characteristic of the device: L[um]=0.6, W[um]=5, aluminium contacts

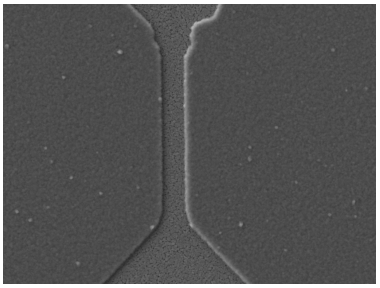

Figure 5.35: SEM image of the device's channel after 100 cycles. Characteristic of the device: L[um]=0.6, W[um]=5, aluminium contacts

Graph 5.36 illustrates the total resistance of devices before and after 100 cycles, specifically for a channel length of 2 um. A similar behavior is observed for devices on both wafers. For both gold and aluminium contacts, an initial cycle displays high resistivity, followed by a significant reduction in resistivity during the second cycle. Subsequently, a progressive increase in resistivity in the insulating regime is noted as the cycles continue.

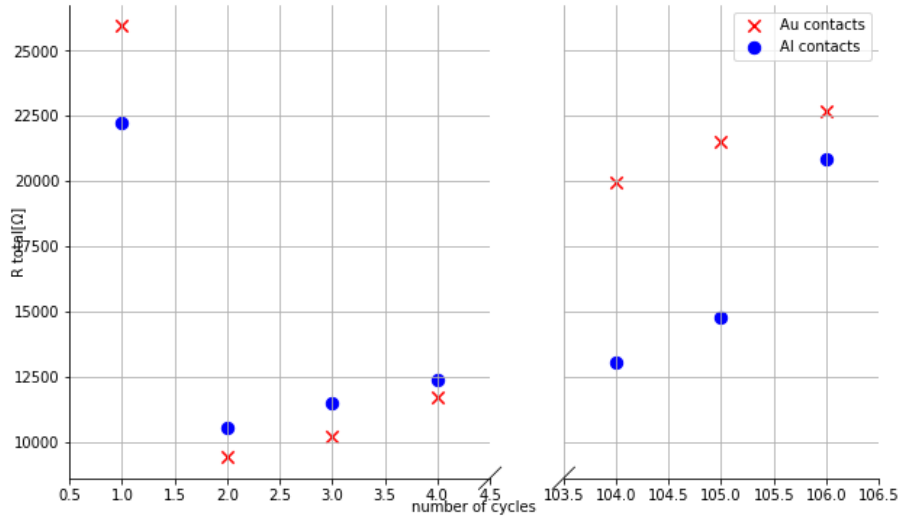

Figure 5.36: Total resistivity measured at 35°C for VO2 with gold and aluminium contacts in function of the number of cycles. Device length L[um]=2, Device width W[um]=5.

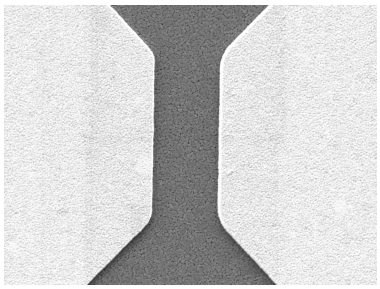

Figure 5.37: SEM image of the pristine device's channel. Characteristic of the device: L[um]=2, W[um]=5, gold contacts

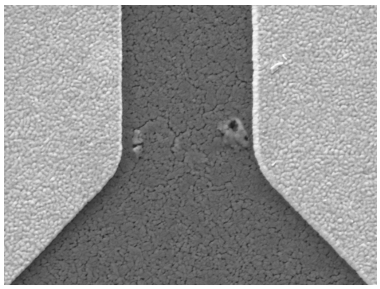

Figure 5.38: SEM image of the device's channel after 1 cycle. Characteristic of the device: L[um]=2, W[um]=5, gold contacts

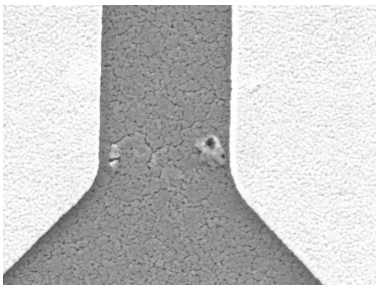

Figure 5.39: SEM image of the device's channel after 100 cycles. Characteristic of the device: L[um]=2, W[um]=5, gold contacts

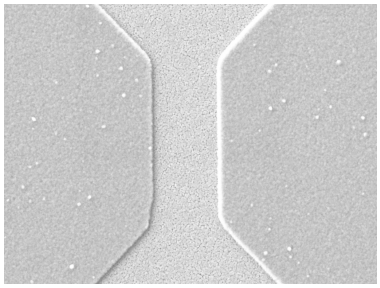

Figure 5.40: SEM image of the pristine device's channel. Characteristic of the device: L[um]=2, W[um]=5, aluminium contacts

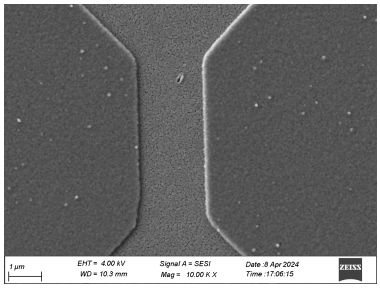

Figure 5.41: SEM image of the device's channel after 1 cycle. Characteristic of the device: L[um]=2, W[um]=5, aluminium contacts

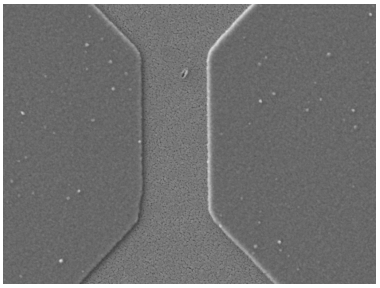

Figure 5.42: SEM image of the device's channel after 100 cycles. Characteristic of the device: L[um]=2, W[um]=5, aluminium contacts

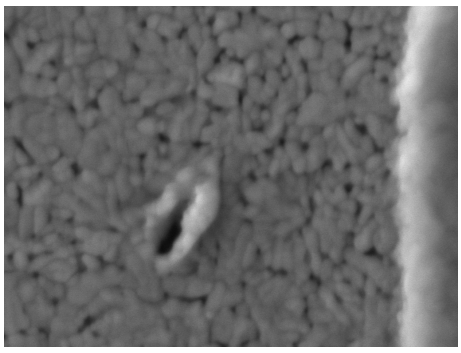

Figure 5.43: Zoom of the device's channel after 100 cycles.5.42

The SEM images ranging from 5.37 to 5.43 depict the surface of the vanadium dioxide layer within the channels (2 um) of the devices. For both gold and aluminium contact devices, the channels appear intact before the cycling process begins. After the first cycle, a slight, permanent modification in the VO2 layer is observed, resembling a small crater on both wafers. However, no further deterioration is evident in the channel when comparing

the images taken after the first cycle 5.38, 5.41 with those taken after 100 cycles 5.39, 5.42.

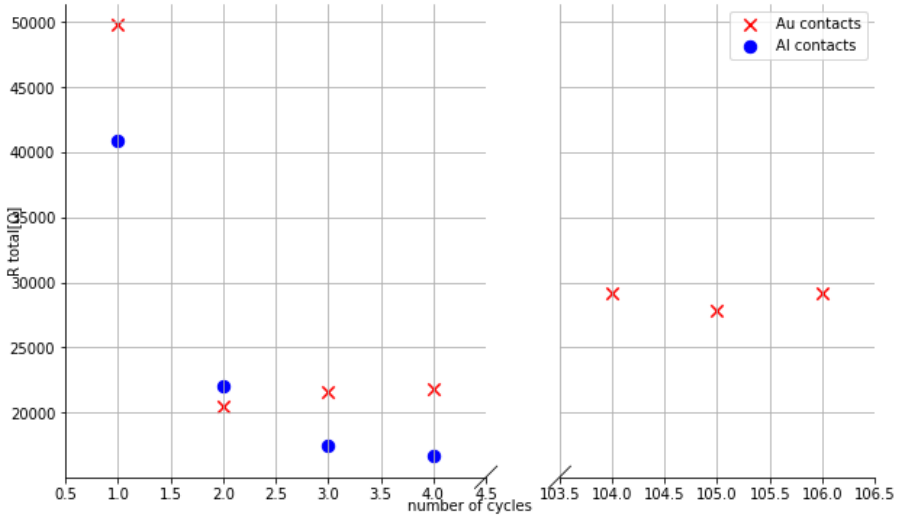

Figure 5.44: Total resistivity measured at 35°C for VO2 with gold and aluminium contacts in function of the number of cycles. Device length L[um]=6, Device width W[um]=5.

As with previous cases, the graph 5.44 illustrates the total resistivity as a function of the number of cycles for devices with 6 um channel lengths. No resistivity values are presented for the aluminium contact device after 100 cycles, as it was unable to transition to a metallic state during the cycling process. A similar trend is observed as with the 2 um channel devices, with an initial high resistivity followed by a significant drop in resistance during subsequent cycles. Additionally, a slight increase in resistance is noted for gold contact devices after the first cycle.

The SEM images from 5.45 to 5.50 reveal substantial deformation in the channels of devices on both wafers starting from the first cycle. This permanent deformation is also evident in the graph 5.44 as a drop in resistivity from the second cycle onward. No additional degradation of the channels is observed after 100 cycles.

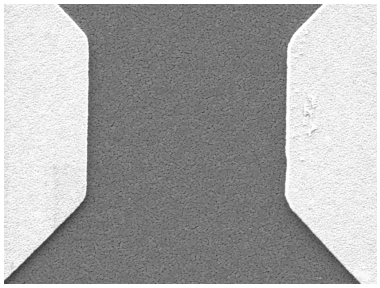

Figure 5.45: SEM image of the pristine device's channel. Characteristic of the device: L[um]=6, W[um]=5, gold contacts

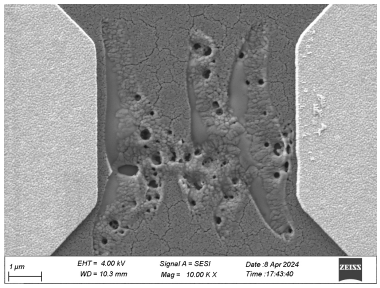

Figure 5.46: SEM image of the device's channel after 1 cycle. Characteristic of the device: L[um]=6, W[um]=5, gold contacts

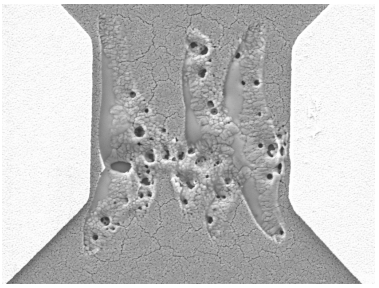

Figure 5.47: SEM image of the device's channel after 100 cycles. Characteristic of the device: L[um]=6, W[um]=5, gold contacts

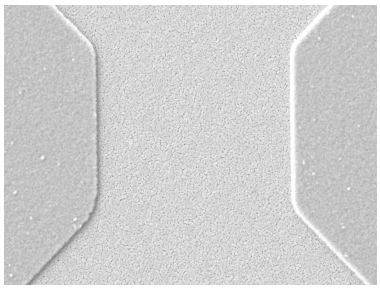

Figure 5.48: SEM image of the pristine device's channel. Characteristic of the device: L[um]=6, W[um]=5, aluminium contacts

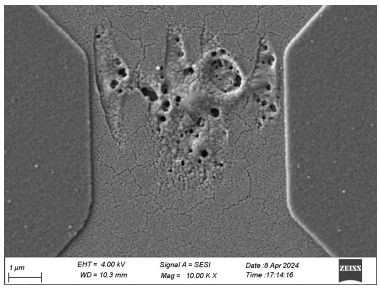

Figure 5.49: SEM image of the device's channel after 1 cycle. Characteristic of the device: L[um]=6, W[um]=5, aluminium contacts

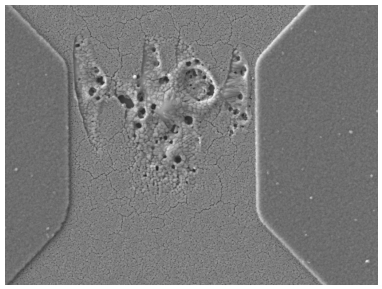

Figure 5.50: SEM image of the device's channel after 100 cycles. Characteristic of the device: L[um]=6, W[um]=5, aluminium contacts

In general, for the tested two-terminal devices, an initial high resistivity is observed, accompanied by changes in the grain structure within the channels. This is followed by a significant drop in resistance, approximately halving by the subsequent cycle. After this, the total resistance gradually and slightly increases with the number of cycles. This effect was observed only after the fourth cycle for the device with gold contacts and a 0.6 um channel length. Conversely, this phenomenon did not occur for the device with aluminium contacts and a 0.6 um channel length, where no structural changes in the grain within the channel were noted and the resistance remained relatively constant throughout the cycles.

Based on the SEM images, it is inferred that the damage observed in the channels after the first cycle is attributable to the current passing through the resistance. This provides an indication of the approximate current path between the two metal contacts and the grains that underwent phase changes.

This first-cycle effect is rarely described and analyzed in the VO2 literature. The thesis [12] also observes these initialization cycles, noting observable and irreversible damage to the VO2 layer. The authors suggest that this effect is due to current spikes caused by the charging of parasitic capacitances upon the abrupt phase transition of the device. The article [38] similarly suggests that the damage arises from current spikes and proposes that reducing these parasitic capacitances could mitigate the damage. Another approach would be to reduce the sharpness of the transition by fabricating composite structures, introducing defects, or triggering the device transitions at temperatures closer to the transition temperature T_c. Indeed, the sharpness of our transitions, characterized in part by the ON/OFF ratio calculated in section 5.2, is high (10^3). Consequently, the current density within the metallic filament will also be elevated. The small-grain devices in the article [3], also fabricated at UCLouvain, do not exhibit a first-cycle effect; however, their ON/OFF ratio was also lower (around 10^2).

Moreover, the geometry of the devices also impacts the first-cycle effect and the associated damage. It has been observed that the longer the channel length, the more significant the damage. This has already been noted in the article [23]. Assuming that these degradations are due to high temperatures in the metallic filament during the transition, devices with longer channels would exhibit higher localized current densities than

those with shorter channels. Indeed, it appears that the current at which the device transitions during the first cycle, leading to damage, is higher for devices with longer channels (see Figures A.15 and A.16). Additionally, the cross-section of the formed filament may potentially depend on the device size and the current during the transition, which would also impact the current density and could explain the differences in damage depending on the channel length [33].

However, the hypothesis made following the results of Protocol 1 cannot be confirmed. Devices with aluminum contacts do not experience more severe or faster degradation compared to those with gold contacts. The significant increase in resistance and the associated damage observed in some aluminum devices can potentially be attributed to device-to-device variability, as these damages do not appear systematically for devices of the same size.

5.3.1 Raman spectroscopy

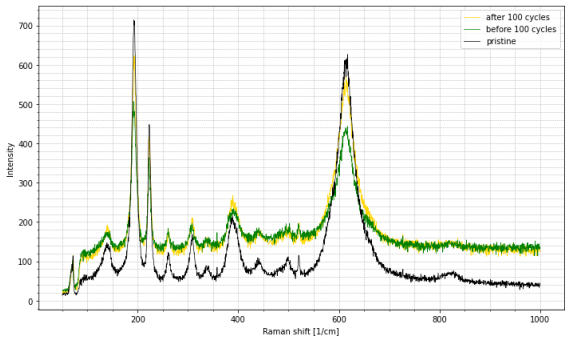

Figure 5.51: Raman spectra of the vanadium layer located in the channel of the devices pristine, after the first cycle and after 100 cycles. Characteristics of the device : L[um]=2, W[um]=5, gold contacts

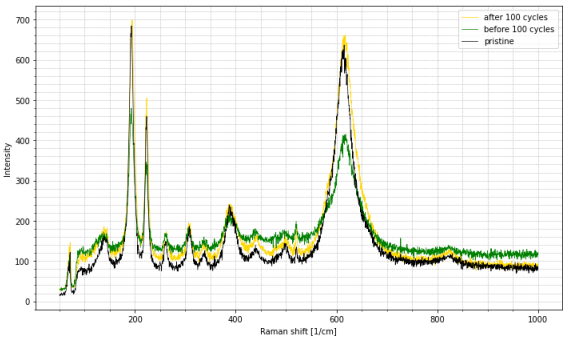

Figure 5.52: Raman spectra of the vanadium layer located in the channel of the devices pristine, after the first cycle and after 100 cycles. Characteristics of the device : L[um]=2, W[um]=5, aluminium contacts

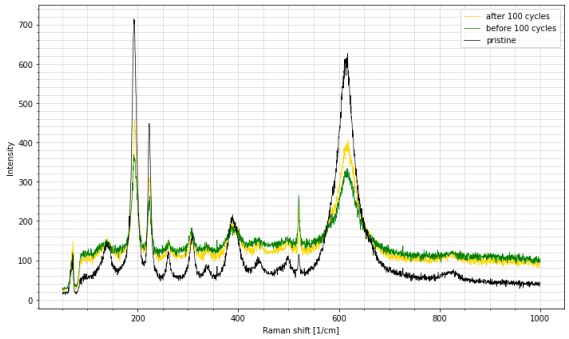

Figure 5.53: Raman spectra of the vanadium layer located in the channel of the devices pristine, after the first cycle and after 100 cycles. Characteristics of the device : L[um]=6, W[um]=5, gold contacts

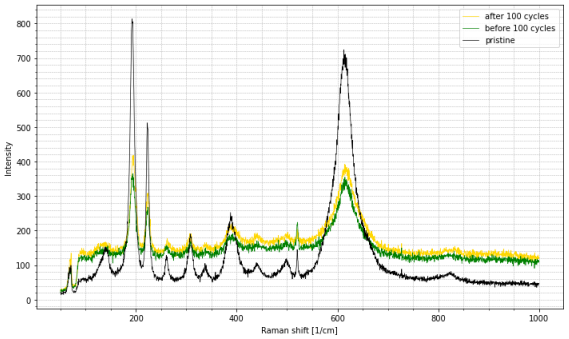

Figure 5.54: Raman spectra of the vanadium layer located in the channel of the devices: pristine, after the first cycle and after 100 cycles. Characteristics of the device : L[um]=6, W[um]=5, aluminium contacts

Figures 5.51, 5.52, 5.53, and 5.54 illustrate the Raman spectra of the VO2 layer measured within the channels of devices with lengths L[um]=2 and 6 on both gold and aluminium wafers. Each graph corresponds to a specific device. In each figure, the black curve represents the Raman spectrum of the VO2 in the channel before any electrical measurements. The green curve represents the spectrum of the VO2 after the first cycle, while the yellow curve represents the spectrum after 100 cycles.

Each graph shows a noticeable offset between the pristine spectrum and the spectra obtained after just one cycle. Furthermore, the peak widths appear to decrease between the pristine measurements and the others, indicating disorder in the material's network structure. This is likely due to the damage sustained within the channels. The article [38] suggests that portions of the film melt, creep due to surface tension, and recrystallize inhomogeneously, which corroborates this hypothesis. Despite this, the VO2 peaks remain discernible on all curves, indicating that vanadium dioxide is still present, even in the device with a 6 um channel and aluminium contacts, which failed to transition during the 100 cycles. However, it is advisable to conduct X-ray diffraction measurements to ensure that there are no changes in stoichiometry, such as the presence of oxygen and vanadium in different forms, across the various spectra.

5.4 Ageing AC

In the ageing tests conducted above, the current was incrementally varied from 0 A to 2 mA (before returning to 0) in small steps. The device thus underwent complete cycles, transitioning from an insulating state to a metallic state before reverting to its insulating state. Achieving 100 cycles was feasible but time-consuming, even at low resolution on the PM8PS, which significantly limited the number of cycles performed. This is far short of the number of cycles that such devices should ideally undergo in future applications 2.1.3.

In most applications, vanadium dioxide resistors are incorporated into circuits where they transition between insulating and metallic states very rapidly (on the order of kHz). To achieve this, a current must be applied that keeps the VO2 within its NDR zone, observable on current-voltage curves during device cycling, while subtly varying the current to switch between states.

To place the devices into this specific operating regime, they were incorporated into a circuit previously developed within the lab prior to this work, as detailed in 5.55.

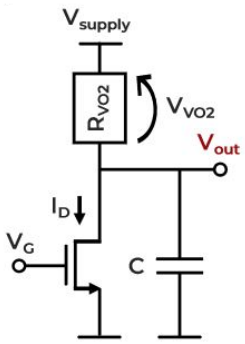

Figure 5.55: schematic of the circuit [4]

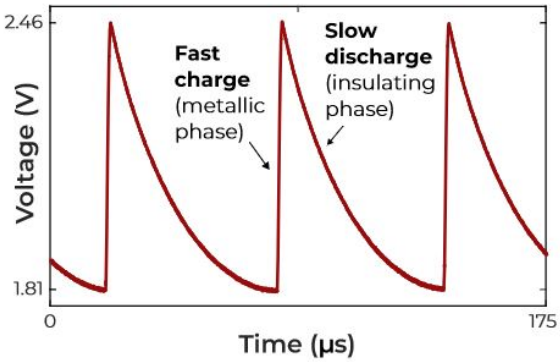

Figure 5.56: Exemple of the response of V_{out} when the circuit is switching ON [4]

The circuit, depicted in Figure 5.55, consists of the VO2 resistor R_{VO2}, an NMOS transistor, and a capacitor c. It includes two voltage sources: one for the supply voltage V_{supply} and another to control the gate voltage of the transistor V_G. By appropriately setting V_G to ensure the NMOS transistor operates in saturation mode, the current I_D is also set, placing it within the negative differential resistance (NDR) region of the resistor. This configuration allows V_{out} to spike, enabling the VO2 resistor to transition multiple times. When the VO2 resistor is in its metallic state, it exhibits low resistance, permitting current flow and charging the capacitor. Consequently, V_{out} increases rapidly, thereby reducing the voltage across the resistor V_{VO2} and decreasing the current through it. As the current decreases, the VO2 resistor returns to its insulating state, allowing only a minimal current to flow. The capacitor then discharges through the transistor, lowering V_{out} and increasing the voltage across the resistor until V_{VO2} reaches a sufficient value to revert the VO2 to a metallic state, thus restarting the described cycle.

Upon installation of the circuit, an attempt was made to induce spiking in V_{out}, indi-

cating that the VO2 alternates continuously between its two states. Various devices with different channel lengths L and widths W were tested. It was observed that devices with smaller lengths and widths were able to sustain this regime for longer durations. Moreover, as the channel length of the devices increases, a higher V_{supply} is required to ensure that the voltage across the resistor is sufficiently high to transition the VO2 to its metallic state. This voltage could potentially damage the transistor due to an excessively high V_{DS}.

An important aspect of the circuit design is the choice of capacitance. The capacitance not only determines the frequency at which V_{out} spikes, through the RC time constant of the circuit, but also affects whether the resistor can maintain the unstable regime of alternating between its two states. If the capacitance is too high, the VO2 remains in its metallic state for an extended period and takes considerable time to revert to its insulating state, suggesting a certain inertia in the metallic state that impedes rapid return to the insulating state. This behavior results in aperiodic and erratic spikes in the output voltage V_{out} and consequently affects the VO2's alternation between its two states.

For these reasons, devices with the smallest sizes, specifically with a channel length L of 0.6 um and a width W of 5 um, were selected from both wafers. The chosen capacitance was 330pF.

By setting the supply voltage V_{supply} to 5 V and gradually increasing the gate voltage V_G to 1.55 V, the VO2 was successfully driven into its unstable regime and transitioned periodically between states on both wafers with gold and aluminium contacts. A spiking frequency of V_{out}, and hence the VO2 transition frequency, was achieved at approximately 100 kHz.

A protocol was defined to analyze the ageing of devices with gold and aluminium contacts. Initially, three high-resolution current-controlled cycles were conducted (4000 steps of 0.5 uA to reach 2 mA and 4000 steps to return to 0) to extract the resistance in the insulating mode of the devices. Subsequently, considering that the devices in circuit 5.55 with the specified parameters transition at a frequency of the order of kHz, it was estimated that 10^8 transitions would be achievable within a reasonable timeframe, providing a preliminary insight into device ageing and potential differences between the two metals used for contacts. To achieve 100 million transitions, a stopwatch was started at the beginning of transitions, and the oscillation frequency was monitored to estimate the required time for 100 million state transitions. The supply voltage was then cut off after the calculated time elapsed. However, upon re-evaluating the frequency at the end of the calculated period, it was noted that the frequency had slightly drifted and decreased over time, resulting in slightly fewer transitions than intended. For the device with gold contacts, at V_{supply} of 5 V and V_G of 1.55 V, a frequency of 132 kHz was observed with an estimated time of 12 minutes and 38 seconds. A frequency of 123 kHz was recorded shortly before the end of this period. For devices with aluminium contacts, under the same parameters, a frequency of 164.5 kHz was obtained with an estimated time of 10 minutes and 8 seconds. The frequency decreased to 157 kHz after 10 minutes. The exact number of VO2 transitions remains uncertain, but it is slightly below 100 million in both cases. Subsequently, the impact of these transitions on the devices was analyzed by conducting three additional current-controlled cycles as previously described, followed by SEM observation to detect any potential damage or other alterations.

#	Steps		
	number of cycles	**measurement type**	**resolution**
1	3	current driven(2mA max)	high (8000 points)
2	approximately 100M	voltage driven	/
3	3	current driven(2mA max)	high (8000 points)
4	/	SEM	/

Table 5.6: Protocol to investigate the ageing of VO2 with gold and aluminium contacts at 308.15K. Dimensions of the device tested : L[um]=0.6 and W[um] = 5.

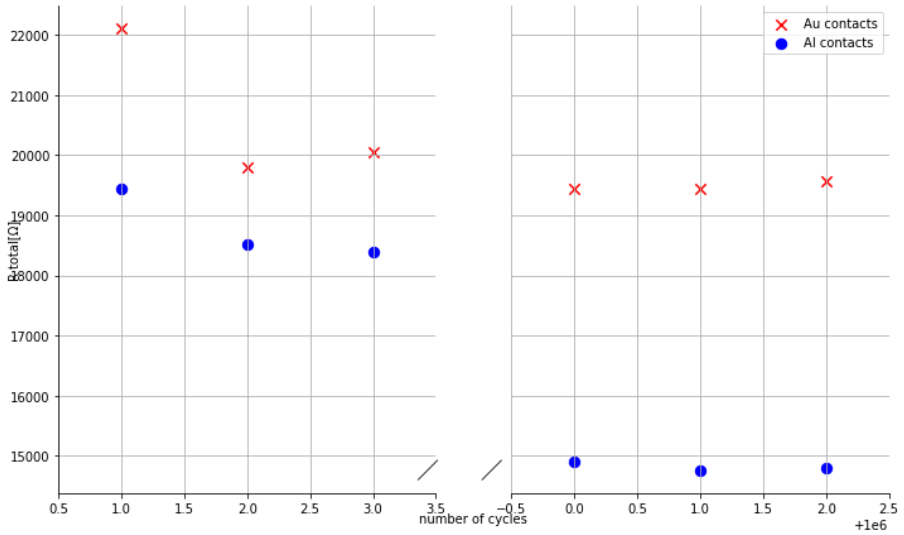

Figure 5.57: Total resistivity measured at 35°C for VO2 with gold and aluminium contacts in function of the number of cycles. Measurements performed in AC. Device length L[um]=6, Device width W[um]=5

As observed in previous DC tests, the graph 5.57 reveals a resistance drop after the first cycle for both devices. This indicates a similar behavior between devices with gold contacts and those with aluminium contacts.Damage is visible in the channel of the device with gold contacts in the SEM image 5.58, likely occurring during the first cycle given the observed drop in resistivity thereafter. However, no apparent damage is observed in the channel of the device with aluminum contacts (Fig 5.59). This explains the fact that the resistance drop is somewhat less pronounced in devices with aluminium contacts. However, in all cases, this reduction is less significant compared to the DC measurements previously recorded. Notably, unlike gold, the resistance in devices with aluminium continues to decrease over millions of transitions. Additionally, the resistance values for both devices appear to stabilize after numerous transitions. Combined with the fact that the devices continue to transition under electrical stimulation, this suggests that aluminium is a viable alternative to gold for the contacts in these devices.

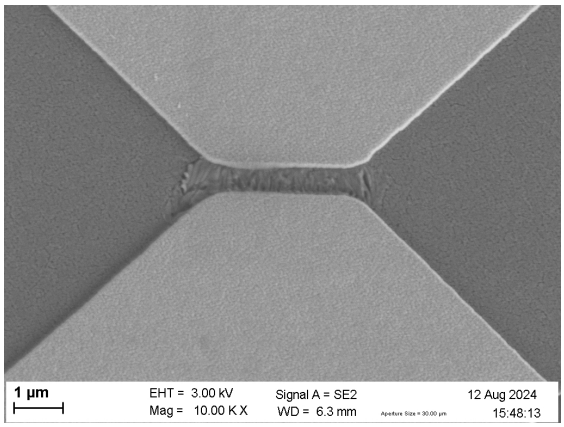

Figure 5.58: SEM image of the device's channel after cycling. Characteristic of the device: L[um]=0.6, W[um]=5, gold contacts

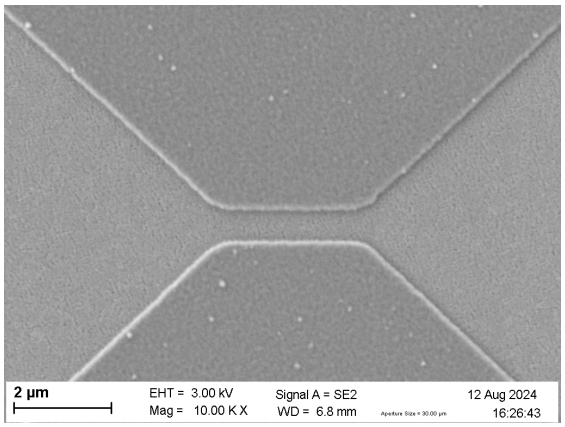

Figure 5.59: SEM image of the device's channel after cycling. Characteristic of the device: L[um]=0.6, W[um]=5, Aluminium contacts

Chapter 6

Conclusion

Previous studies [37][2] have highlighted that the use of gold as a contact material in the fabrication process of vanadium-based devices is the most energy-intensive step, thereby contributing the most to equivalent greenhouse gas emissions. This is primarily due to the extraction and manufacturing of gold, which represents the main cause of this high footprint. The objective of this thesis was therefore to identify and analyze a potential alternative to gold as a contact material in this process.

This work begins with a literature review on vanadium dioxide, describing its noteworthy properties. The key interest in VO2 lies in its ability to transition from an insulating to a metallic state at 68°C. This transition, the origin of which is still debated, can also be electrically triggered through the Joule effect or by charge carrier injection. This property holds significant promise for applications, particularly in the field of neuromorphic systems. The variability of these devices is then presented, along with the damage that can be observed in certain cases. The review concludes with a focus on metallic contacts.

The reasons behind the choice of aluminium as an alternative contact material for the devices are then explained. Subsequently, each step of the vanadium dioxide device fabrication process is described, with the basic principle of each step outlined before listing the parameters used for the wafers with gold and aluminium contacts.

Once the devices were fabricated, characterization began with the observation of VO2 using microscopy and Raman spectroscopy. Electrical characterization followed, ensuring that the devices exhibited a clear transition between the insulating and metallic phases. The sheet resistance of VO2 on the two wafers was characterized using four-point measurements, and the contact resistance of the two metals was analyzed through TLM measurements. Given the applications of VO2 that require a high number of transitions, and considering the challenges of recycling metals from PCBs due to the minute quantities present, the aging of the devices and its impact on the different contact metals was studied. Initial results suggesting more significant or at least faster aging for devices with aluminium contacts prompted further rigorous investigation. Measuring resistance revealed the emergence of a highly resistive first cycle, indicative of deformations in the VO2 channel, followed by a decrease in resistivity in subsequent cycles. This is caused by

the sudden formation of metallic filaments in the channel during the transition, generating intense heat through the Joule effect. It is hypothesized that this effect is amplified by a high ON/OFF ratio. It was also observed that longer channels result in more significant damage. However, it was found that devices with aluminium contacts do not degrade more quickly than those with gold. Finally, the devices were introduced into a circuit to induce an unstable state where VO2 rapidly alternates between its two states. This circuit enabled approximately 100 million transitions. Resistance measurements again revealed an initial cycle effect with higher resistance, although the subsequent voltage drop was less pronounced than in DC cycles. Damage was observed in the VO2 channel with gold, but no apparent deformation was seen in the channel with aluminium. The resistance values of the devices stabilized after these millions of cycles.

Several observations were made in conclusion. Firstly, the devices with aluminium contacts successfully transitioned, even under AC conditions with millions of cycles. Additionally, the post-cycle resistance values appeared stable, confirming the hypothesis that aluminium can be a viable alternative contact material, drastically reducing the CED and GHG emissions of the VO2 device fabrication process. Secondly, the presence of a highly resistive first cycle followed by a decrease in resistivity in subsequent cycles was repeatedly observed. This is attributed to degradation in the VO2 channel caused by intense heat from the formation of metallic filaments during the transition, which significantly increases the current density and the Joule effect at the filament's location. It is hypothesized that this is due to the high ON/OFF ratio of the devices and their dimensions. Finally, significant cycle-to-cycle and device-to-device variability were observed, making the interpretation of results challenging.

In conclusion, this work provides hope for finding viable alternatives to gold contacts. This is important in the context of climate urgency and given the ecological footprint of gold. However, this work is only the beginning of characterizing VO2 devices with aluminium contacts. Much remains to be investigated, whether concerning the nature of the VO2 transition, the variability of these devices, or the nature of the highly resistive first cycles observed.

Appendix A

Appendices : Caracterisation

A.1 Observation

A.1.1 Raman

VO	V2O3 (thermal)	V2O3 (sputtering from V target on SiO2/Si sample)	V3O5 (sputtering from V2O3 target on SiO2/Si sample)	VO2 (M1) (thermal)	VO2 (M1) (thermal) on SiO2/Si	VO2 (M1) (sputtering from V target) thin film deposited on SiO2	VO2 (M1) (sputtering from V target on SiO2/Si sample)	VO2 (T) (sputtering from V target on SiO2/Si sample)	VO2 (M2) (sputtering from V target on SiO2/Si sample)	VO2 (R)	V6O13 (thermal)	V6O13 (sputtering from V target on SiO2/Si sample)	VTO16 + alpha-V2O5 (thermal) structure	VTO16 + V3O7 (sputtering from V target on SiO2/Si sample)	V3O7	alpha-V2O5 (thermal/sol)	alpha-V2O5 (sputtering from V target on SiO2/Si sample)
Shvets 2019	Shvets 2019	Shvets 2019	Shvets 2019	Shvets 2019	Ferrari 2017	Zhang 2016	Shvets 2019	Shvets 2019	Shvets 2019	Shvets 2019	Shvets 2019	Shvets 2019	Shvets 2019	Shvets 2019	Shvets 2019	Shvets 2019	Shvets 2019
Peak (cm-1)	Peak (cm-1)	Peak (cm-1)	Peak (cm-1)	Peak (cm-1)	Peak (cm-1)	Peak (cm-1)	Peak (cm-1)	Peak (cm-1)	Peak (cm-1)	Peak (cm-1)	Peak (cm-1)	Peak (cm-1)	Peak (cm-1)	Peak (cm-1)	Peak (cm-1)	Peak (cm-1)	Peak (cm-1)
No Raman data experimentally reported	218	213	155	137	140			135	120	240 (weak & broad)	94	85	70	80	835	107	104
	240	237	183	143		144	143	193	202	390 (weak & broad)	137	127	155	105	848	147	146
	300	297	194	194	192	193	193	224	220	510 (weak & broad)	188	133	251	130	881	149	199
	340	328	223	224	223	223	224	261	228	625 (weak & broad)	275	155	695	163	871	200	286
	378		274	262	260	260	261	310	270		300	196	841	193	924	201	304
	510	503	282	310	308	308	310	339	275		403	206	880	224	932	236	405
	600	586	294		338	334	339	385	298		457	239	929	261	1021	290	484
			304	393	387	389	391	391	304		520	269	981	299	1028	291	702
			321		395			399	373		684	283	1027	341		310	995
			337	442	440		443	443 (increased)	412		840	300		425		315	
			373				449	449	436		990	337		494		350	
			405	484	482		482 (small shoulder)	482 (increased)	453			344		543		404	
			418	499	497	497		585	572			367		691		483	
			462	582	588		590 (small shoulder)	590	646			422		789		507	
			487	612	613	613	614	614	830			502		848		526	
			563	663	661		665 (small shoulder)	619				674		879		702	
			593	820	823		824 (very weak)	665				700		914		963	
			641					824 (increased)				846		943		992	
			670									918		987			
			738											1027			

Figure A.1: Differents known peaks of differents Vanadium oxides found in the literature[39]

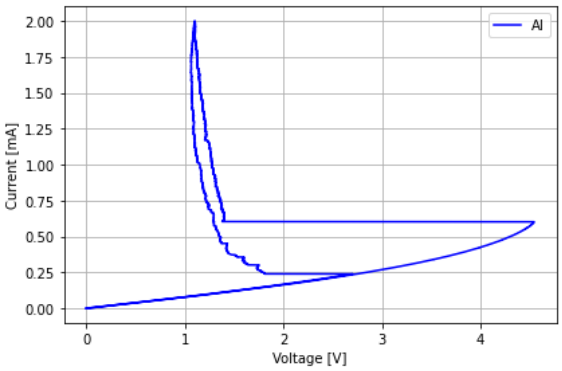

Figure A.2: First cycle completed at high resolution (4000 points) for the device with aluminium contacts at 308.15K. The length of the device L[um]=1.2 and the width W[um]=15

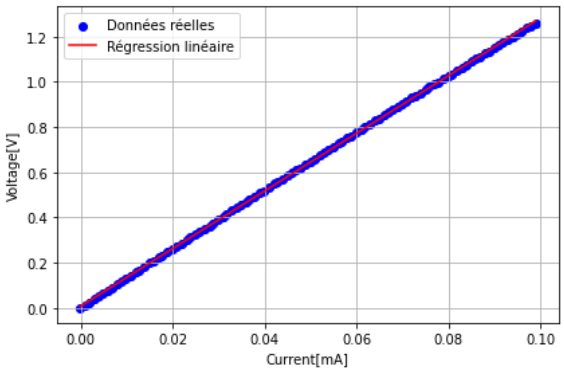

Figure A.3: linear regression of the 100 first points of the first cycle in order to extract the insulating resistance A.2

A.2 Proper functionning

A.3 Ageing DC

A.3.1 first protocol

SEM images

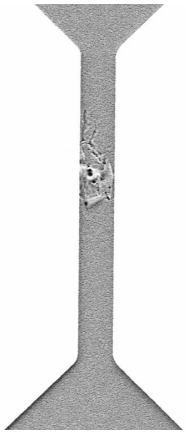

Figure A.4: SEM image of the device's channel after 100 cycles. Characteristic of the device: L[um]=1.6, W[um]=15, gold contacts

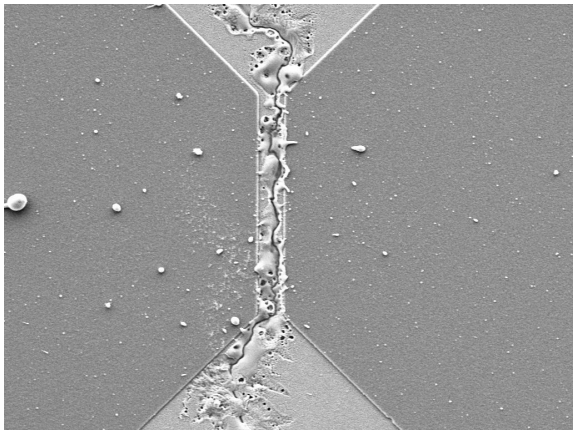

Figure A.5: SEM image of the device's channel after 100 cycles. Characteristic of the device: L[um]=1.6, W[um]=15, aluminium contacts

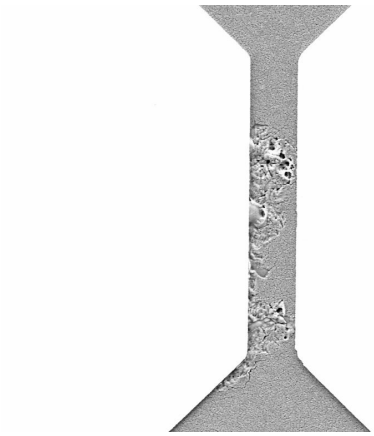

Figure A.6: SEM image of the device's channel after 100 cycles. Characteristic of the device: L[um]=2.4, W[um]=15, gold contacts

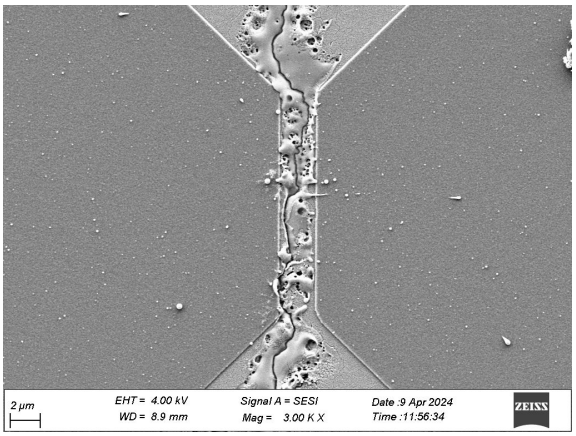

Figure A.7: SEM image of the device's channel after 100 cycles. Characteristic of the device: L[um]=2.4, W[um]=15, aluminium contacts

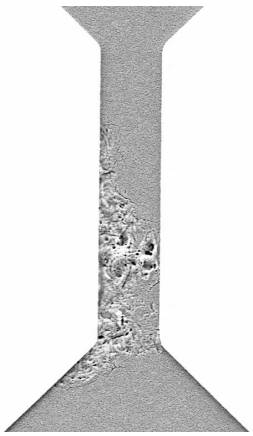

Figure A.8: SEM image of the device's channel after 100 cycles. Characteristic of the device: L[um]=3, W[um]=15, gold contacts

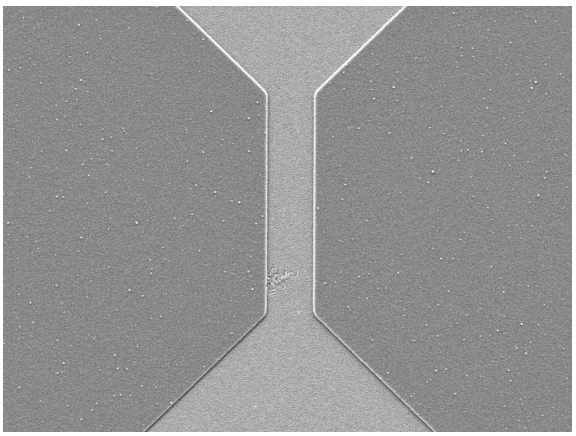

Figure A.9: SEM image of the device's channel after 100 cycles. Characteristic of the device: L[um]=3, W[um]=15, aluminium contacts

A.3.2 second protocol

I-V curves (Voltage driven)

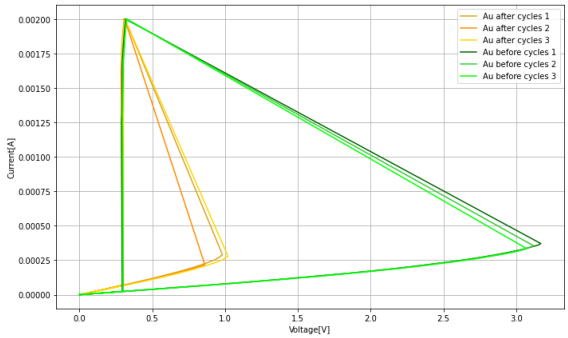

Figure A.10: I-V curve in Voltage driven (see Table 5.5). Characteristic of the device: L[um]=0.6, W[um]=5, gold contacts

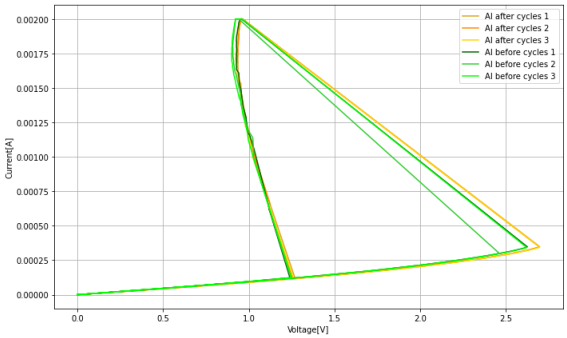

Figure A.11: I-V curve in Voltage driven (see Table 5.5). Characteristic of the device: L[um]=0.6, W[um]=5, Aluminium contacts

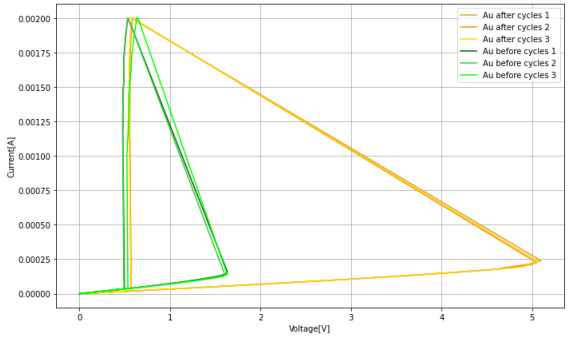

Figure A.12: I-V curve in Voltage driven (see Table 5.5). Characteristic of the device: L[um]=2, W[um]=5, gold contacts

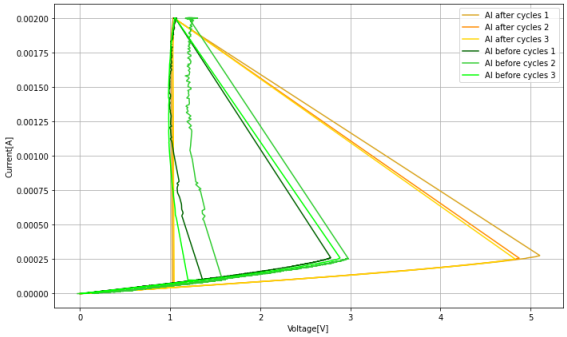

Figure A.13: I-V curve in Voltage driven (see Table 5.5). Characteristic of the device: L[um]=2, W[um]=5, Aluminium contact

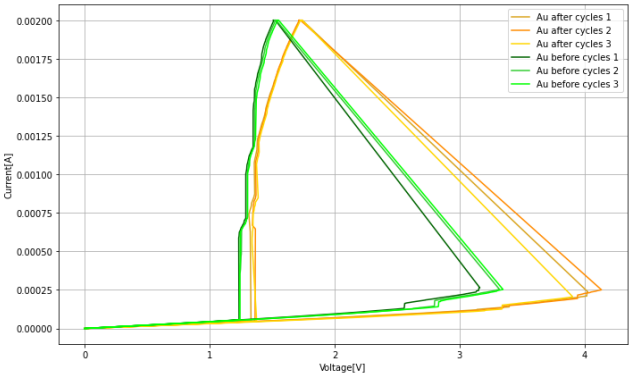

Figure A.14: I-V curve in Voltage driven (see Table 5.5). Characteristic of the device: L[um]=6, W[um]=5, gold contacts

I-V curves (Current driven)

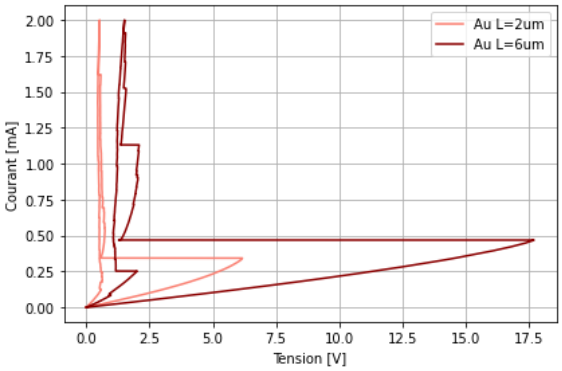

Figure A.15: I-V curve of the first transition in current driven (see Table 5.5). Characteristic of the devices: L[um]=2 and L[um]=6, W[um]=5, gold contacts

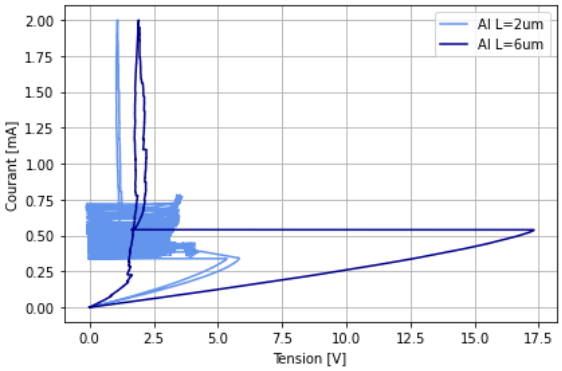

Figure A.16: I-V curve of the first transition in current driven (see Table 5.5). Characteristic of the devices: L[um]=2 and L[um]=6, W[um]=5, Aluminium contacts

Bibliography

[1] Ph.D. Anne Marie Helmenstine. *Table of Electrical Resistivity and Conductivity*. 2023. URL: https://www.greelane.com/fr/science-technologie-math%C3%A9matiques/science/table-of-electrical-resistivity-conductivity-608499.

[2] Noemie Bidoul et al. "Process-based Life Cycle Assessment of a Vanadium Dioxide Spiking Neuron". In: ().

[3] Noémie Bidoul, Nicolas Roisin, and Denis Flandre. "Tuning the Intrinsic Stochasticity of Resistive Switching in VO2 Microresistors". In: *Nano Letters* 24.21 (2024), pp. 6201–6209. DOI: 10.1021/acs.nanolett.4c00184.

[4] Noémie Bidoul et al. "Static and Dynamic Stochastic Analysis of a Temperature-Sensitive VO 2 Spiking Neuron". In: *ESSDERC 2023 - IEEE 53rd European Solid-State Device Research Conference (ESSDERC)*. Lisbon, Portugal: IEEE, 2023, pp. 81–84. DOI: 10.1109/ESSDERC59256.2023.10268509. URL: https://doi.org/10.1109/ESSDERC59256.2023.10268509.

[5] Lizzie Boakes et al. "Selection of Alternative Local Interconnect Metals: Beyond Traditional Criteria Towards Sustainable and Secure Supply Chains". In: *Proceedings of the Royal Society of London. Series A, Mathematical and Physical Sciences* (2024). Accessed: August 18, 2024. URL: https://doi.org/10.1098/rspa.1951.0231.

[6] Patrick K. Bowen. "Basic Theory of Contact Resistance". In: *Tech Briefs, Deringer Ney* (2020). URL: https://deringerney.com/basic-theory-contact-resistance.

[7] Tianci Chang et al. "Mitigating Deterioration of Vanadium Dioxide Thermochromic Films by Interfacial Encapsulation". In: *Matter* 1.3 (Sept. 2019), pp. 734–744. DOI: 10.1016/j.matt.2019.04.004. URL: https://doi.org/10.1016/j.matt.2019.04.004.

[8] Shuguang Cheng et al. "Investigation of work function and surface energy of aluminum: An ab-initio study". In: *2013 IEEE 5th International Nanoelectronics Conference (INEC)*. 2013, pp. 473–475. DOI: 10.1109/INEC.2013.6466081.

[9] Wikipedia contributors. *Contact resistance*. 2024. URL: https://en.wikipedia.org/wiki/Contact_resistance.

[10] Wikipedia contributors. *Metal–semiconductor junction: Schottky–Mott rule and Fermi level pinning*. 2024. URL: https://en.wikipedia.org/wiki/Metal%E2%80%93semiconductor_junction#Schottky%E2%80%93Mott_rule_and_Fermi_level_pinning.

[11] Wikipedia contributors. *Ohmic contact*. 2024. URL: https://en.wikipedia.org/wiki/Ohmic_contact.

[12] Elisabetta Corti. "Networks of Coupled VO2 Oscillators for Neuromorphic Computing". PhD Thesis. Lausanne: École Polytechnique Fédérale de Lausanne (EPFL), Apr. 2021, p. 154. DOI: 10.5075/epfl-thesis-9303. URL: https://infoscience.epfl.ch/handle/20.500.14299/177371.

[13] Edinburgh Instruments. *What is Raman Spectroscopy?* 2024. URL: https://www.edinst.com/fr/blog/what-is-raman-spectroscopy/.

[14] FindLight. *AR Coating Techniques*. 2024. URL: https://www.findlight.net/blog/ar-coating-techniques/.

[15] Humaira Ghazal and Nadeem Sohail. "Sputtering Deposition". In: *Thin Films*. Ed. by Dongfang Yang. Rijeka: IntechOpen, 2022. Chap. 2. DOI: 10.5772/intechopen.107353. URL: https://doi.org/10.5772/intechopen.107353.

[16] Patricia Guarnieri et al. "Recycling Challenges for Electronic Consumer Products to E-Waste: A Developing Countries' Perspective". In: *E-waste Recycling and Management: Present Scenarios and Environmental Issues*. Ed. by Anish Khan, Inamuddin, and Abdullah M. Asiri. Cham: Springer International Publishing, 2020, pp. 81–110. ISBN: 978-3-030-14184-4. DOI: 10.1007/978-3-030-14184-4_5. URL: https://doi.org/10.1007/978-3-030-14184-4_5.

[17] Dany Hachem et al. "Variation de la résistance de contact métal/semi-conducteur dans une structure HEMT GaN sous illumination UV". In: *Symposium de Génie Electrique (SGE 2018)*. 4p. ffhal-02981923v2f. Université de Lorraine [UL]. Nancy, France, July 2018.

[18] Chuan Yu Han et al. "Characterization and Modelling of Flexible VO2 Mott Memristor for the Artificial Spiking Warm Receptor". In: *Advanced Materials Interfaces* 9.19 (July 2022), p. 2200394. DOI: 10.1002/admi.202200394. URL: https://doi.org/10.1002/admi.202200394.

[19] Ulrich Hilleringmann. "Oxidation of Silicon". In: *Silicon Semiconductor Technology: Processing and Integration of Microelectronic Devices*. Wiesbaden: Springer Fachmedien Wiesbaden, 2023, pp. 21–32. ISBN: 978-3-658-41041-4. DOI: 10.1007/978-3-658-41041-4_3. URL: https://doi.org/10.1007/978-3-658-41041-4_3.

[20] Christiana Honsberg and Stuart Bowden. *Four Point Probe Resistivity Measurements*. URL: https://www.pveducation.org/pvcdrom/characterisation/four-point-probe-resistivity-measurements.

[21] Christiana Honsberg and Stuart Bowden. *TLM Measurement*. URL: https://www.pveducation.org/pvcdrom/tlm-measurement.

[22] Jingsourcing. *Types of Physical Vapor Deposition (PVD)*. 2024. URL: https://jingsourcing.com/p/b04-types-of-physical-vapor-deposition/.

[23] Arash Joushaghani et al. "Voltage-Controlled Switching and Thermal Effects in VO2 Nano-Gap Junctions". In: *Applied Physics Letters* 104 (2014), p. 221904. URL: https://api.semanticscholar.org/CorpusID:122041922.

[24] Kwan Chi Kao. "Ohmic Contacts". English. In: *Comprehensive Semiconductor Science and Technology*. Copyright © 2004 Elsevier Inc. All rights reserved. Academic Press, 2004. ISBN: 978-0-12-396561-5. DOI: 10.1016/B978-0-12-396561-5.X5010-5. URL: https://doi.org/10.1016/B978-0-12-396561-5.X5010-5.

[25] LibreTexts. *B1: Workfunction Values (Reference Table)*. Accessed: August 18, 2024. 2021. URL: https://chem.libretexts.org/Ancillary_Materials/Reference/Reference_Tables/Bulk_Properties/B1%5C%3A_Workfunction_Values_(Reference_Table).

[26] D. Liu et al. "Effects of Microdefects and Grain Size on the Phase Transition Properties of Nano-VO2(M)". In: *Journal of Solid State Chemistry* 288 (2020), p. 121450.

[27] Y. Liu et al. "Effect of Annealing Temperature on the Structure and Properties of Vanadium Oxide Films". In: *Optical Materials Express* 6.5 (2016), p. 1552.

[28] R. Marassi and F. Nobili. "MEASUREMENT METHODS | Structural and Chemical Properties: Scanning Electron Microscopy". In: *Encyclopedia of Electrochemical Power Sources*. Ed. by Jürgen Garche. Amsterdam: Elsevier, 2009, pp. 758–768. ISBN: 978-0-444-52745-5. DOI: https://doi.org/10.1016/B978-044452745-5.00071-X. URL: https://www.sciencedirect.com/science/article/pii/B978044452745500071X.

[29] Margaret McNair. "Contact Resistance Reduction – A Path to Greater Electrical Efficiency". In: (2023). URL: https://www.electricalcontactsint.com/post/contact-resistance-reduction-a-path-to-greater-electrical-efficiency.

[30] LNF Wiki University of Michigan. *Four Point Probe*. URL: https://lnf-wiki.eecs.umich.edu/wiki/Four_point_probe.

[31] Edgar William John Mitchell and John Wesley Mitchell. "The work functions of copper, silver and aluminium". In: *Proceedings of the Royal Society of London. Series A, Mathematical and Physical Sciences* 210 (1951), pp. 70–84. DOI: 10.1098/rspa.1951.0231. URL: http://doi.org/10.1098/rspa.1951.0231.

[32] Joyeeta Nag and R. F. Haglund. "Synthesis of vanadium dioxide thin films and nanoparticles". In: *Journal of Physics: Condensed Matter* 20.26 (2008), p. 264016. ISSN: 0953-8984. DOI: 10.1088/0953-8984/20/26/264016.

[33] Sanjoy Kumar Nandi et al. "Understanding modes of negative differential resistance in amorphous and polycrystalline vanadium oxides". In: *Journal of Applied Physics* 128.24 (Dec. 2020), p. 244103. ISSN: 0021-8979. DOI: 10.1063/5.0027875. eprint: https://pubs.aip.org/aip/jap/article-pdf/doi/10.1063/5.0027875/15257532/244103_1_online.pdf. URL: https://doi.org/10.1063/5.0027875.

[34] C. Ni. "Scanning Electron Microscopy (SEM)". In: *Encyclopedia of Tribology*. Ed. by Q.J. Wang and Y.W. Chung. Boston, MA: Springer, 2013. DOI: 10.1007/978-0-387-92897-5_1217. URL: https://doi.org/10.1007/978-0-387-92897-5%5C_1217.

[35] Microbe Notes. *Scanning Electron Microscope (SEM)*. 2021. URL: https://microbenotes.com/scanning-electron-microscope-sem/.

[36] Philipp Nuss and Matthew J. Eckelman. "Life cycle assessment of metals: a scientific synthesis". In: *PLoS One* 9.7 (2014), e101298. DOI: 10.1371/journal.pone.0101298. URL: https://doi.org/10.1371/journal.pone.0101298.

[37] Pauline Raux. "Joint evaluation of performance and environmental impacts of a microfabricated device. VO2-based device". Accessed: 2024-08-15. Master's thesis. Louvain-la-Neuve, Belgium: Université catholique de Louvain, 2023. URL: http://hdl.handle.net/2078.1/thesis:40552.

[38] Anatoly G. Shabalin et al. "Nanoimaging of Electrical Failure in VO2 Resistive-Switching Nanodevices". In: *ACS Applied Electronic Materials* 2.8 (2020), pp. 2357–2362. DOI: 10.1021/acsaelm.0c00382. eprint: https://doi.org/10.1021/acsaelm.0c00382. URL: https://doi.org/10.1021/acsaelm.0c00382.

[39] P. Shvets et al. "A review of Raman spectroscopy of vanadium oxides". In: *J Raman Spectrosc* 50 (2019), pp. 1226–1244. DOI: 10.1002/jrs.5616. URL: https://doi.org/10.1002/jrs.5616.

[40] Thermo Fisher Scientific. *Raman Spectroscopy Academy*. 2024. URL: https://www.thermofisher.com/be/en/home/industrial/spectroscopy-elemental-isotope-analysis/molecular-spectroscopy/raman-microscopy/resources/raman-spectroscopy-academy.html.

[41] Javier del Valle et al. "Spatiotemporal characterization of the field-induced insulator-to-metal transition". In: *Science* 373.6557 (2021), pp. 907–911. DOI: 10.1126/science.abd9088. eprint: https://www.science.org/doi/pdf/10.1126/science.abd9088. URL: https://www.science.org/doi/abs/10.1126/science.abd9088.

[42] Javier del Valle et al. "Generation of Tunable Stochastic Sequences Using the Insulator–Metal Transition". In: *Nano Letters* 22.3 (2022). PMID: 35061947, pp. 1251–1256. DOI: 10.1021/acs.nanolett.1c04404. eprint: https://doi.org/10.1021/acs.nanolett.1c04404. URL: https://doi.org/10.1021/acs.nanolett.1c04404.

[43] Qi Wang et al. "Environmental data and facts in the semiconductor manufacturing industry: An unexpected high water and energy consumption situation". In: *Water Cycle* 4 (2023), pp. 47–54. ISSN: 2666-4453. DOI: https://doi.org/10.1016/j.watcyc.2023.01.004. URL: https://www.sciencedirect.com/science/article/pii/S2666445323000041.

[44] G. Windred. "Electrical contact resistance". In: *Journal of the Franklin Institute* 231.6 (1941), pp. 547–585. ISSN: 0016-0032. DOI: https://doi.org/10.1016/S0016-0032(41)90159-X. URL: https://www.sciencedirect.com/science/article/pii/S001600324190159X.

[45] Ke Yang et al. "High-order sensory processing nanocircuit based on coupled VO2 oscillators". In: *Nature Communications* 15.1 (Feb. 2024), p. 1693. ISSN: 2041-1723. DOI: 10.1038/s41467-024-45992-8. URL: https://doi.org/10.1038/s41467-024-45992-8.

[46] N. Yuan et al. "The large modification of phase transition characteristics of VO2 films on SiO2/Si substrates". In: *Thin Solid Films* 515.4 (2006), pp. 1275–1279.

[47] Rui Yuan et al. “A Calibratable Sensory Neuron Based on Epitaxial VO2 for Spike-Based Neuromorphic Multisensory System”. In: *Nature Communications* 13.1 (July 2022), p. 3973. DOI: 10.1038/s41467-022-31747-w. URL: https://doi.org/10.1038/s41467-022-31747-w.

UNIVERSITÉ CATHOLIQUE DE LOUVAIN
École polytechnique de Louvain
Rue Archimède, 1 bte L6.11.01, 1348 Louvain-la-Neuve, Belgique | **www.uclouvain.be/epl**